

Inner ear biomechanics reveals a Late Triassic origin for mammalian endothermy

<https://doi.org/10.1038/s41586-022-04963-z>

Received: 28 May 2021

Accepted: 10 June 2022

Published online: 20 July 2022

 Check for updates

Ricardo Araújo^{1,2,17} , Romain David^{3,4,17} , Julien Benoit⁵, Jacqueline K. Lungmus⁶, Alexander Stoessel^{4,7}, Paul M. Barrett³, Jessica A. Maisano⁸, Eric Ekdale^{9,10}, Maëva Orliac², Zhe-Xi Luo¹¹, Agustín G. Martinelli¹², Eva A. Hoffman¹³, Christian A. Sidor¹⁴, Rui M. S. Martins¹, Fred Spoor^{3,4,15} & Kenneth D. Angielczyk¹⁶ 

Endothermy underpins the ecological dominance of mammals and birds in diverse environmental settings^{1,2}. However, it is unclear when this crucial feature emerged during mammalian evolutionary history, as most of the fossil evidence is ambiguous^{3–17}. Here we show that this key evolutionary transition can be investigated using the morphology of the endolymph-filled semicircular ducts of the inner ear, which monitor head rotations and are essential for motor coordination, navigation and spatial awareness^{18–22}. Increased body temperatures during the ectotherm–endotherm transition of mammal ancestors would decrease endolymph viscosity, negatively affecting semicircular duct biomechanics^{23,24}, while simultaneously increasing behavioural activity^{25,26} probably required improved performance²⁷. Morphological changes to the membranous ducts and enclosing bony canals would have been necessary to maintain optimal functionality during this transition. To track these morphofunctional changes in 56 extinct synapsid species, we developed the thermo-motility index, a proxy based on bony canal morphology. The results suggest that endothermy evolved abruptly during the Late Triassic period in Mammaliaformes, correlated with a sharp increase in body temperature (5–9 °C) and an expansion of aerobic and anaerobic capacities. Contrary to previous suggestions^{3–14}, all stem mammaliamorphs were most probably ectotherms. Endothermy, as a crucial physiological characteristic, joins other distinctive mammalian features that arose during this period of climatic instability²⁸.

Excluding short and long-term torpor, endotherms ('warm-blooded' animals) can maintain high (31–45 °C) and nearly constant body temperature^{1,2} (T_b), mostly through metabolic heat production. By contrast, ectotherms ('cold-blooded' animals) depend on environmental temperatures, detrimentally affecting their lifestyle²⁹, although some can elevate their T_b slightly above ambient levels through incipient heat production or active behavioural thermoregulation^{30–32} (Supplementary Note 1). Compared with ectotherms, endotherms are more behaviourally active, show increased aerobic capacity, travel further and achieve higher locomotor speeds, at the expense of higher energy costs^{1,2,25,33,34} (Supplementary Note 2 and Supplementary Data 1). Consequently, extant mammals and birds occupy a wide variety of ecological niches unrivalled by other vertebrates. Endothermy is a quintessentially mammalian feature, intimately related to other hallmarks such as sweat glands and fur^{1,2}. However, its evolution remains one of the great unsolved mysteries of palaeontology^{1,2}. Lines of evidence invoked

to identify the emergence of mammalian endothermy rely mostly on skeletal anatomical features, but also on ichnological, osteohistological and isotopic information, which have been used as correlates for aerobic capacity^{3,5}, basal metabolic rate^{4,6,13,15}, thermal insulation^{8,16}, parental care⁹, nocturnality¹² and body temperature^{7,10}. Most of these features are poorly sampled in the fossil record, have not been linked directly to T_b , and often cannot be interpreted as unambiguous markers for endothermy. In addition, the origins of many of these features were not concomitant^{1–17}, making it difficult to pinpoint at which node of the evolutionary tree mammalian ancestors could be considered endotherms.

The thermo-motility index is a proxy for T_b

Here we show that the functional morphology of the semicircular duct system (SDS) of the inner ear provides new, independent insights that

¹Instituto de Plasmas e Fusão Nuclear, Instituto Superior Técnico, Universidade de Lisboa, Lisboa, Portugal. ²Institut des Sciences de L'Évolution de Montpellier, Université de Montpellier, Montpellier, France. ³Natural History Museum, London, UK. ⁴Max Plank Institute for Evolutionary Anthropology, Leipzig, Germany. ⁵Evolutionary Studies Institute, University of Witwatersrand, Johannesburg, South Africa. ⁶Department of Paleobiology, National Museum of Natural History, Washington DC, USA. ⁷Institute of Zoology and Evolutionary Research, Friedrich Schiller University Jena, Jena, Germany. ⁸Jackson School of Geosciences, University of Texas at Austin, Austin, TX, USA. ⁹Department of Biology, San Diego State University, San Diego, CA, USA. ¹⁰Department of Paleontology, San Diego Natural History Museum, San Diego, CA, USA. ¹¹Department of Organismal Biology and Anatomy, University of Chicago, Chicago, IL, USA. ¹²Museo Argentino de Ciencias Naturales 'Bernardino Rivadavia', Buenos Aires, Argentina. ¹³Division of Paleontology, American Museum of Natural History, New York, NY, USA. ¹⁴Burke Museum and Department of Biology, University of Washington, Seattle, WA, USA. ¹⁵Department of Anthropology, University College London, London, UK. ¹⁶Neguanee Integrative Research Center, Field Museum of Natural History, Chicago, IL, USA. ¹⁷These authors contributed equally: Ricardo Araújo, Romain David. e-mail: Ricardo.araujo@tecnico.ulisboa.pt; r.david@nhm.ac.uk; kangielczyk@fieldmuseum.org

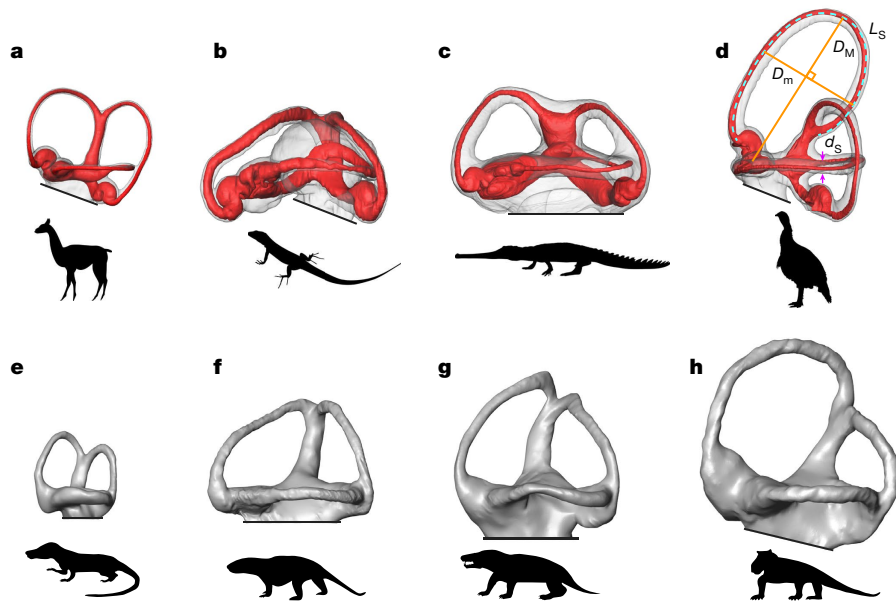


Fig. 1 | Three-dimensional visualizations of bony and membranous labyrinths. **a–d**, Lateral views of the upper part of the bony labyrinth (grey) and the membranous semicircular duct system (red) of an alpaca (**a**; CEB 130038), a Sicilian wall lizard (**b**; CEB 130040), a false gharial (**c**; CEB140070) and a domestic turkey (**d**; CEB 130069). **d**, Illustration of measurements of major (D_M) and minor (D_m) axes of the semicircular canal torus, cross-sectional thickness (d_s) and length (L_s) of the slender portion. **e–h**, Lateral views of the

upper part of the bony labyrinth of *Tritylodon* (**e**; BP/1/4778), *Trirachodon* (**f**; BP/1/4658), *Microgomphodon* (**g**; SAM-PK-10160) and *Lemurosaurus* (**h**; BP/1/816). All labyrinths have been scaled relative to body size, according to the average relative size of the groups. Animal silhouettes were either created by R.A. (**e,f,h**) or are available at Phylopic (<http://phylopic.org/>) under a Public Domain license (**a–d,g**).

help to solve this problem. Semicircular ducts monitor head rotation and are filled with endolymph, a fluid whose viscosity affects function and depends on T_b . Perception of head motion is essential for navigation²², balance²¹, vision²⁰, motor coordination²¹ and spatial awareness²¹. Therefore, SDS function is expected to attune to the spectrum of head rotations (that is, angular velocities and ordinary frequencies) experienced by an organism²⁷. In this context, endotherms not only need to compensate for the decreased response speed (that is, decreased upper corner frequency) induced by the lower endolymph viscosity^{23,24} associated with elevated T_b ^{23,24}, but may also require a more efficient SDS than ectotherms (Supplementary Methods) because they are more active on average^{1,2,25,26,33,34}. Optimal SDS function can be achieved by modifying endolymph chemistry to increase its viscosity and/or altering SDS morphology.

To track these adaptations in the fossil record, we developed the thermo-motility index (TMI), a biomechanically informed proxy derived primarily from functionally relevant morphometric parameters of the SDS and corrected for allometry (Supplementary Methods). The TMI is defined so that for a given body size, relevant SDS function = TMI + a temperature term (inversely related to T_b). T_b does not contribute to the calculation of the TMI. Nevertheless, measuring the TMI should enable prediction of T_b , because assuming that SDS function is attuned to natural head motion, an increase in T_b (reducing the temperature term) should be proportionally compensated by an increase in the TMI. Similarly, because the TMI is positively related to maximum angular head motion (Methods and Supplementary Methods), when behavioural activity increases, the TMI may have to increase to improve SDS function. As the SDS does not fossilize, we assembled a new dataset of 50 membranous labyrinths of various vertebrates to establish morphofunctional correlations between semicircular ducts and bony canals (Supplementary Data 2 and Supplementary Note 2). Subsequently, we computed the TMI of 362 specimens, including 68 extinct synapsids, from bony labyrinths visualized through microtomography (Fig. 1, Extended Data Fig. 1 and 2 and Supplementary Data 2 and 3).

Empirical testing of TMI accuracy

We demonstrated empirically that the TMI is explained by and positively correlated to T_b (Fig. 2, solid curve; phylogenetic generalized least-squares regression (PGLS), relative likelihood against null model = 1.00; Supplementary Note 2). Among the semicircular canals, the TMI of the anterior canal, which shows the highest correlation with T_b , is better explained by T_b for clades than species (species: $n = 230$, adjusted $R^2 = 0.07$; clades: $n = 28$, adjusted $R^2 = 0.86$). This suggests that other explanatory variables affecting head motion and/or SDS performance (for example, behavioural ecology³⁵, bauplan²⁷ and visual acuity³⁶) drive morphological variation at the species level and blur the correlation (Supplementary Note 2). Consequently, reversing the relationship to predict T_b from the TMI gives more accurate results for clades than for species (species: $n = 230$, adjusted $R^2 = 0.01$; clades: $n = 28$, adjusted $R^2 = 0.86$; Supplementary Note 2). Notably, the relationship between the TMI and T_b shows a steeper increase than would be theoretically expected from compensation only for temperature-induced changes in viscosity (Fig. 2b, dashed curve). This steeper-than-expected increase probably reflects a positive correlation between overall head motion and T_b (Supplementary Note 2). This corollary is congruent with the aerobic capacity model³⁴ in that elevated T_b in endotherms may not have evolved in isolation, but in tandem with increased aerobic capacity, translating into increased behavioural activity. At high-ranking taxonomic levels, T_b may explain the size differences observed among the SDS of vertebrates²⁷ when body size is accounted for.

The TMI of extant endotherms is significantly higher than that of extant ectotherms (PGLS ANOVA, endotherms: $n = 143$, ectotherms: $n = 127$, adjusted $R^2 = 0.06$, Glass' $\Delta = 1.77$ with 95% confidence interval [1.48–2.06], $P = 2.57 \cdot 10^{-5}$; Supplementary Note 2). Fishes, amphibians and turtles show the lowest T_b , which are reflected by their low TMI values (Fig. 2). Conversely, birds and mammals show the highest TMI, in agreement with their higher T_b . Crocodilians and lepidosaurs are intermediate between these extremes. In tetrapods, the TMI shows a significant negative correlation with canal cross-sectional thickness

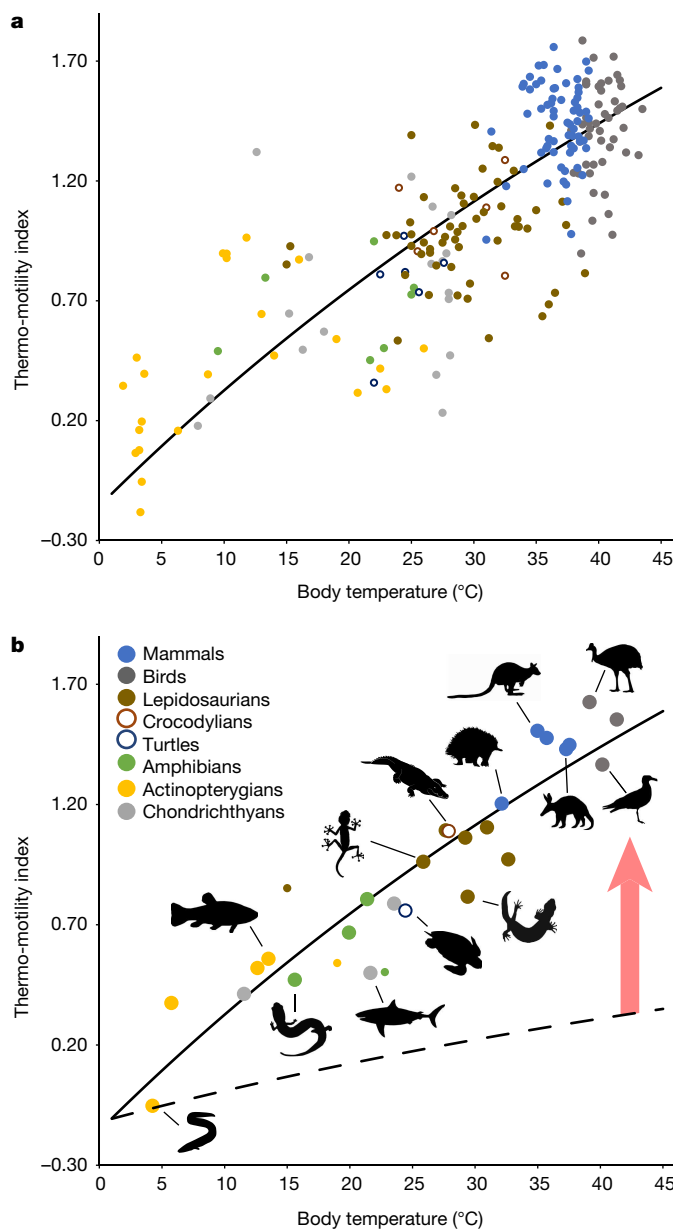


Fig. 2 | Relationships between the TMI and body temperature. **a, b**, Scatter plot for individual species (**a**) and when combined in major groups of vertebrates (**b**). The dashed curve represents the theoretical relationship when T_b affects only endolymph viscosity and not behavioural activity. The solid curve represents the empirical relationship for the major groups of vertebrates, taking phylogeny into account. The difference between the two curves (red arrow) suggests that, in addition to the TMI, T_b is also positively correlated with head motion, further increasing the TMI. Animal silhouettes were either created by R.A. (eel and gecko) or are available at Phylopic (<http://phylopic.org/>) under a Public Domain license.

relative to the radius of curvature and the radius of curvature relative to body mass (Supplementary Note 2). Among extant species, mammals show the lowest values for relative cross-sectional thickness and relative radius of curvature (Extended Data Fig. 3), leading to high TMI values. However, birds have semicircular canals with large relative radii of curvature and relative cross-sectional thicknesses that are average for amniotes (Extended Data Fig. 3). In this context, to attain their high TMI values, birds responded differently to increased T_b by modifying aspects of their membranous labyrinth and the physicochemical properties of their endolymph³⁷ (Extended Data Fig. 4) while maintaining

plesiomorphic bony labyrinth dimensions. The TMI distributions of ectotherms and endotherms show little overlap (Fig. 3), indicating that this metric could be useful for assessing the thermoregulatory regime of extinct organisms.

Phylogenetic origin of mammalian endothermy

To understand the thermophysiology of fossil synapsids, we computed body temperature distributions from the TMI of fossil specimens, using Brownian motion simulations calibrated with extant data (Supplementary Note 2), and calculated the probabilities of endothermy for each fossil taxon and node by fitting a phylogenetic logistic regression to the TMI distribution of extant species (Fig. 3, Table 1, Extended Data Figs. 5 and 6 and Extended Data Tables 1–3). We obtained a cross-validated error rate of 5% by using this regression to classify the thermoregulatory regime of extant species and clades, when regarding probabilities for species ($P > 0.70$) and for clades ($P > 0.53$) indicating endothermy, and for species ($P < 0.30$) and clades ($P < 0.47$) implying ectothermy, as well as intermediate probabilities as expressing uncertainty. In this framework, maximum-likelihood ancestral state reconstruction shows that the clade threshold for endothermy is crossed at the Mammaliamorpha node ($P = 0.70$), and non-mammalian mammaliamorphs are the only non-mammalian synapsids classified as endotherms (Extended Data Tables 1–3). This clade includes all descendants of the last common ancestor of tritylodontids and mammals³⁸ and its origin is currently calibrated at approximately 233 million years ago (Ma), during the Carnian pluvial episode. The TMI of non-mammalian mammaliamorphs (1.29 ± 0.18 (\pm s.d.), non-mammalian mammaliamorphs: $n = 9$) is intermediate between the TMI measured in extant *Ornithorhynchus* (1.25) and that of *Tachyglossus* (1.41). These monotremes are capable of producing their own body heat while inactive but show low basal metabolic rates, relatively low T_b (31–34 °C) and periodic torpor^{33,39}. Mammaliamorphs were probably characterized by this thermoregulatory strategy, defined as basoendothermy¹, with a predicted T_b of approximately 34 °C (95% confidence interval [31.3–36.6]; Table 1 and Extended Data Fig. 5), and behavioural activity that was probably intermediate between extant ectotherms and endotherms (Extended Data Fig. 7). Conversely, all non-mammalian synapsid groups classify as ectotherms, with probabilities below the clade threshold for ectothermy ($P = [0.13–0.36]$), and predicted T_b between 24–29 °C (95% confidence interval [21.9–31.6 °C]; Table 1 and Extended Data Table 3), a range that overlaps with extant turtles, lepidosaurs and crocodilians.

Caveats and literature comparisons

Predictions of body temperature and thermoregulatory regime are subject to uncontrolled parameters affecting the TMI (that is, endolymph chemistry and residual variation of bony/membranous correlations). However, these parameters remained stable on average along the mammalian lineage, between the nodes of Amniota and Mammalia (Extended Data Fig. 4 and Supplementary Note 2). This suggests that thermoregulatory regimes estimated at different nodes within the mammalian lineage are accurately predicted by the bony labyrinth of fossil synapsids. However, we cannot exclude that outbranching synapsid clades (for example, bidentalian dicynodonts^{6,10}) could have independently evolved much thinner membranous semicircular ducts than expected from their bony canals (for example, Phocidae⁴⁰) and/or modified endolymph chemistry toward increased viscosity (for example, European plaice²³) to maintain SDS function. Similarly, we cannot exclude that these organisms could have been much less active than is typical for their size (for example, *Zaglossus*⁴¹). Each of these scenarios would have resulted in T_b at the upper tail of distributions predicted for these clades (Extended Data Fig. 5), generally below 31 °C and significantly lower than predicted for Mammaliamorpha (Table 1).

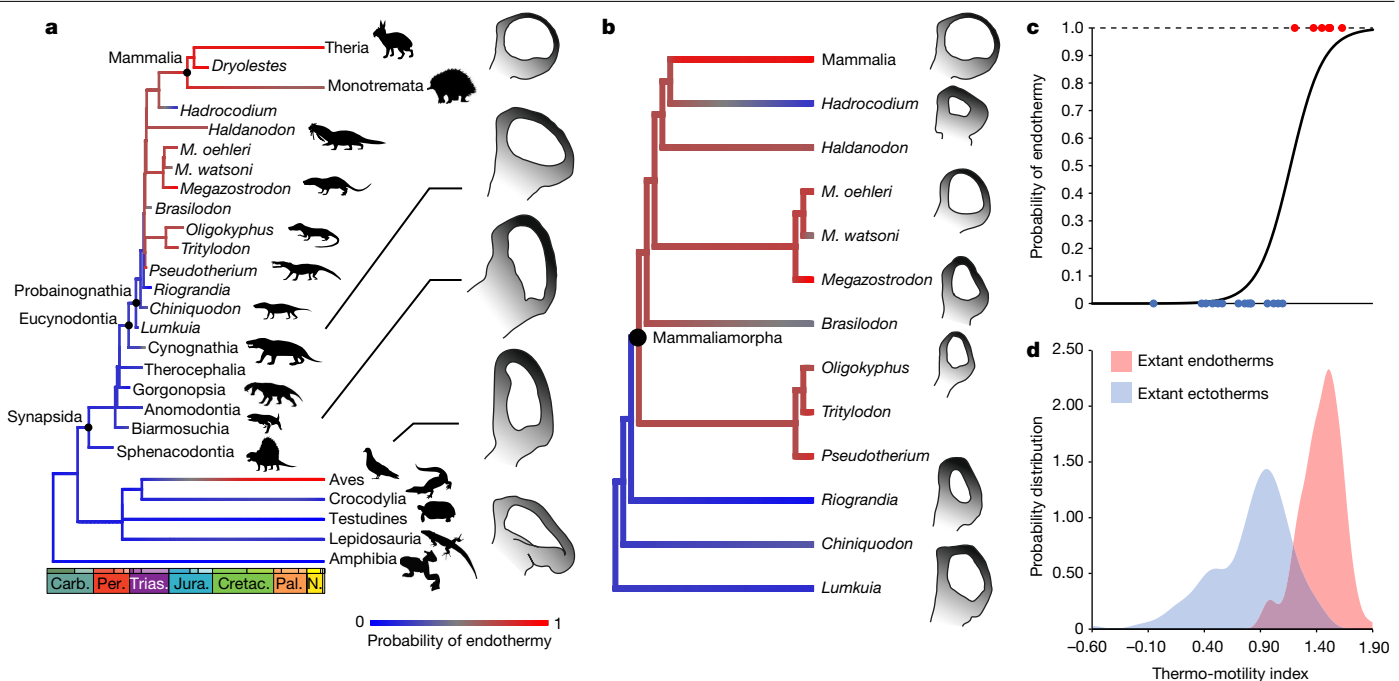


Fig. 3 | Phylogenetic distribution of the TMI in tetrapods. **a,b**, Optimization of the TMI onto a time-calibrated tree of major tetrapod clades (**a**), with expanded detail on the cladogram of probainognathians (**b**). Anterior semicircular canals of example specimens are depicted and scaled to body size. Branch colours reflect the likelihood of being endothermic according to the probability colour scale. *M. oehleri*, *Morganucodon oehleri*; *M. watsoni*, *Morganucodon watsoni*. **c**, Probability of endothermy calculated from a phylogenetic logistic regression computed from the TMI of extant amniotes.

Major groups of extant vertebrates are shown as dots. **d**, Distribution of the TMI for extant endotherms in red and ectotherms in blue. Animal silhouettes were either created by R.A. (*Chiniquodon*, *Megazostrodon*, *Morganucodon*, *Oligokyphus*, *Pseudotherium*, *Anomodontia*, *Cynognathia* and *Sphenacodontia*) or are available at Phylopic (<http://phylopic.org/>) under a Public Domain license. Carb., Carboniferous; Cretac., Cretaceous; Jura., Jurassic; N., Neogene; Pal., Palaeogene; Per., Permian; Trias., Triassic.

Our sample includes some taxa analysed in previous studies using stable oxygen isotopes¹⁰ and osteohistologically inferred metabolic rates⁶. Our evidence is largely consistent with these studies in interpreting sphenacodontians, biarmosuchians, dinocephalians, basal dicynodonts and therocephalians as ectotherms^{6,10}, and in predicting increased T_b in cynognathians¹⁰ (28.9 °C, 95% confidence interval

[26.3–31.6 °C]). As mentioned previously, interpreting results from the TMI of individual fossil taxa rather than clades can be misleading. For example, although the clade Cynognathia is clearly interpreted as ectothermic in our analysis ($P = 0.36$), probabilities of individual species do not enable unambiguous classification (Extended Data Tables 1 and 3).

Table 1 | Predicted body temperatures of groups of non-mammalian synapsids.

Group	Species, n	Specimens, n	T_b (°C)	$P(T_b \geq 31^\circ\text{C})$	$P(T_b \geq \text{Mammaliamorph } T_b)$
Non-mammalian mammaliamorphs	9	11	33.9 [31.3–36.6]	0.87	1.00
Non-mammaliamorph probainognathians	3	3	25.1 [22.4–27.9]	0.02	0.00
Cynognathians	5	5	28.9 [26.3–31.6]	0.21	0.04
Non-eucynodont cynodonts	4	6	27.8 [25.3–30.4]	0.11	0.01
Therocephalians	6	7	24.2 [21.9–26.6]	0.00	0.00
Gorgonopsians	5	5	26.1 [23.7–28.6]	0.03	0.00
Anomodonts	16	19	26.0 [23.9–28.1]	0.01	0.00
Non-neotherapsid therapsids	5	6	26.6 [24.2–29.0]	0.04	0.01
Non-therapsid synapsids	2	2	25.7 [22.4–29.2]	0.07	0.02

Numbers in square brackets represent the confidence intervals of predicted T_b . Numbers in bold represent probabilities significantly excluding T_b higher than or equal to 31°C, or higher than or equal to T_b of non-mammal mammaliamorphs obtained during the same simulations.

Tempo and mode in evolution of endothermy

To investigate evolutionary tempo, we fitted different evolutionary models to the TMI of synapsids (for example, Brownian motion, continuous trend, early burst; Supplementary Note 2). The best-supported model corresponds to partial Brownian motion (that is, Pagel's $\lambda = 0.5$), with a major shift in evolutionary rate in the branch leading to Mammaliaform (Fig. 4). This shift is interpreted as the transition to endothermy, with a change in T_b of $+5\text{--}9\text{ }^\circ\text{C}$ (Table 1) compared with non-mammaliaform eucynodonts. Notably, all models incorporating gradual evolution of the TMI are rejected, as is a change of evolutionary rate after the end-Permian mass extinction, despite other major effects of this extinction⁴². The acquisition of endothermy in Mammaliaform seems to be temporally and phylogenetically consistent with a pulse in brain enlargement¹⁷, the development of respiratory turbinals⁷, the evolution of infraorbital canals (related to the presence of vibrissae¹⁶) and functional differentiation of the vertebral column⁴³, and occurred during the miniaturization process that started in probainognathians¹⁴⁴. However, the acquisitions of parasagittal posture³, the diaphragm⁵, microvascularization⁴, fibrolamellar bone¹³ and parental care⁹ might all have predated the onset of endothermy. These features probably mark gradual stochastic increases in T_b (up to $+3\text{--}4\text{ }^\circ\text{C}$ in eucynodonts, similar to the difference between crocodiles and geckos) and behavioural activity during the evolution of non-probaibgnathian synapsids. Although our sample is small ($n = 3$), our simulations suggest that this gradual stochastic increase stopped in non-mammaliaform probainognathians (Supplementary Note 2), which probably reverted to plesiomorphic synapsid body temperatures (Table 1). This may be explained by the onset of miniaturization⁴⁴, coupled with exploration of low-temperature niches (for example, nocturnality or mesic environments). Combining our results on TMI evolution with physiological and experimental information from extant analogues, we posit that endothermy emerged from the combination of heat production through sarcolipin-mediated thermogenesis and thermal insulation via pelage, which seem essential in mammals to reach and maintain high T_b when exposed to cold^{31,45,46}. The *sln* gene, which controls sarcolipin-mediated thermogenesis, is synapomorphic for vertebrates but has been found to be expressed in mammals, the opah and is suspected to be expressed in birds⁴⁶. Fossil evidence from early Late Jurassic docodonts (for example, *Castorocauda*) and haramiyids (for example, *Maiopatagium*) suggests that pelage could have originated much earlier. Thus, although any of these features could have had an earlier origin, endothermy may have emerged from their combination in Mammaliaform^{1,47}, providing them a selective advantage to cope with a progressively cooler Triassic climate²⁸ in the context of reduced thermal inertia from miniaturization⁴⁴. Despite being spatiotemporally biased⁴⁸, the fossil record indeed seems to suggest that local mammaliaform species richness increased during the Rhaetian cool interval⁴⁹, the coldest time during the Triassic period.

Paleobiology of ectothermic synapsids

Extinct ectotherms depended on environmental temperatures and adopted a wide array of strategies to attain their preferred T_b under varying climatic conditions throughout the year and across latitudes. Despite major palaeoclimatic fluctuations from the middle Permian to the Late Triassic period²⁸, the average preferred T_b (and thus TMI) of non-mammaliaform synapsids remained relatively stable (Fig. 4 and Table 1), suggesting they used different thermoregulatory strategies depending on their local climates (Supplementary Data 4). Considering their palaeoequatorial distribution, sampled non-therapsid synapsids living in tropical climates probably adopted a nocturnal¹² passive thermoconformer lifestyle (for example, geckos³²). Conversely, most sampled middle to late Permian therapsids, living at high palaeolatitudes in the African Karoo, were probably diurnal, using behavioural

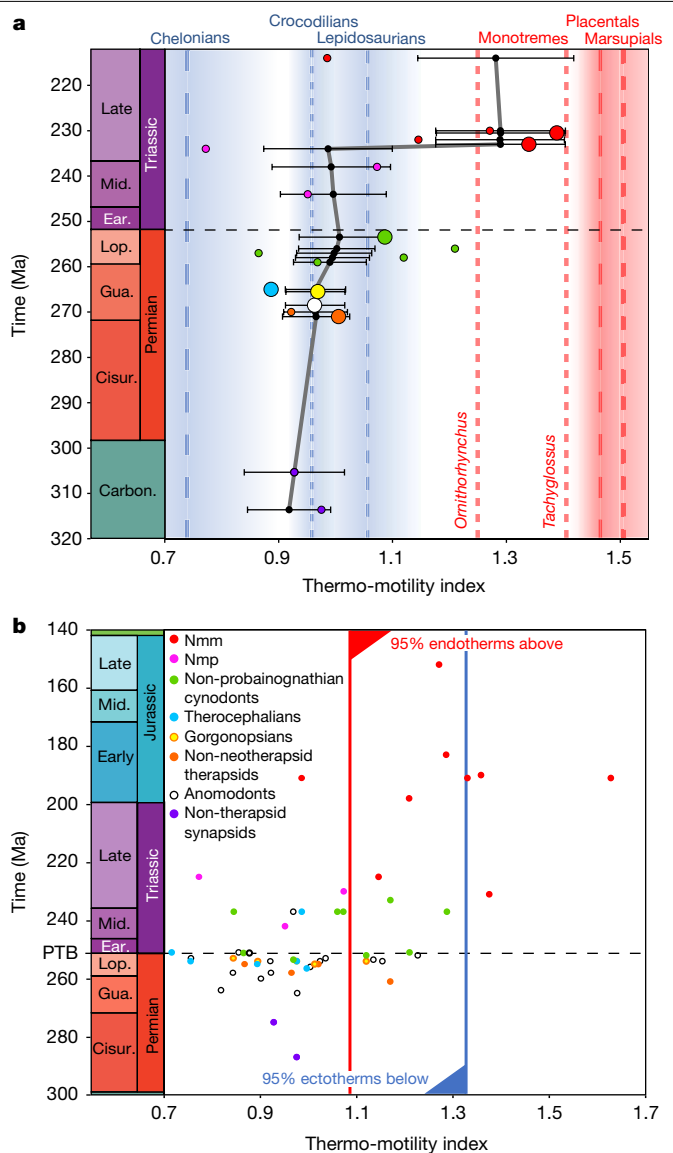


Fig. 4 | Temporal distribution of the TMI in synapsids. **a**, **b**, Scatter plots of geological time against TMI for nodes along the mammalian lineage and clades branching out (a) and for individual species (b). Geological age corresponds to the node origin for clades branching out (a) and last appearance datum for species (b). The black dashed line represents the Permo-Triassic boundary. **a**, The grey line represents the evolution of the TMI along the mammalian lineage. Black dots represent the most likely ancestral state of the TMI at the nodes with 95% confidence intervals (error bars), both computed from a phylogeny containing $n = 67$ tips (Supplementary Note 2 and Supplementary Fig. 53). Large and small dots represent means of major clades (tritylodontids: $n = 3$, morganucodontids: $n = 3$, cynognathians: $n = 5$, therocephalians: $n = 6$, gorgonopsians: $n = 5$, anomodonts: $n = 16$, biarmosuchians: $n = 4$) and individual species, respectively. Dashed lines and shaded areas represent the mean and s.e.m., respectively, of the TMI of example extant endotherm (red) and ectotherm (blue) clades (chelonians: $n = 6$, crocodilians: $n = 9$, lepidosaurians: $n = 61$, placentals: $n = 67$, marsupials: $n = 5$) and the TMI value for monotreme species, excluding specimens outside the 95% confidence interval of these thermoregulatory regimes. **b**, Solid lines represent 95% thresholds of the distribution of the TMI of extant endotherms (red, $n = 145$) and ectotherms (blue, $n = 132$) analysed in this study. Carbon, Carboniferous; Cisur., Cisuralian; Ear., early; Gua., Guadalupian; Lop., Lopingian; Mid., middle; PTB, Permo-Triassic Boundary; Nmm, non-mammal mammaliaforms; Nmp, non-mammal probainognathians.

thermoregulatory strategies to some extent. Furthermore, they must have resorted to long-term torpor during unfavourable periods of the cold season, congruent with histological evidence of cyclical growth¹³ and burrowing⁵⁰. Similarly, during the exceptionally high temperatures of the Early Triassic period, sampled non-eucynodont therapsids were probably forced to aestivate⁵⁰ and/or to become nocturnal.

Conclusions

The thermal budget of vertebrates results from a complex interplay between internally generated heat and heat gained or lost at the body surface. Although inferring the thermoregulatory regime of extinct species can be complicated for these reasons, we use the TMI to demonstrate that a sharp shift to endothermy most probably occurred at the base of Mammaliaformes, accompanied by expanded aerobic and anaerobic capacities and increased body temperatures. The Late Triassic emergence of the physiology and bauplan characterizing mammals was a decisive step that facilitated their evolutionary radiation during the Mesozoic Era and subsequent major ecological expansion during the Cenozoic Era.

Online content

Any methods, additional references, Nature Research reporting summaries, source data, extended data, supplementary information, acknowledgements, peer review information; details of author contributions and competing interests; and statements of data and code availability are available at <https://doi.org/10.1038/s41586-022-04963-z>.

1. Lovegrove, B. G. *Fires of Life: Endothermy in Birds and Mammals* (Yale Univ. Press, 2019).
2. Benton, M. J. The origin of endothermy in synapsids and archosaurs and arms races in the Triassic. *Gondwana Res.* **100**, 261–289 (2021).
3. Kubo, T. & Benton, M. J. Tetrapod postural shift estimated from Permian and Triassic trackways. *Palaeontology* **52**, 1029–1037 (2009).
4. Huttenlocker, A. K. & Farmer, C. G. Bone microvasculature tracks red blood cell size diminution in Triassic mammal and dinosaur forerunners. *Curr. Biol.* **27**, 48–54 (2017).
5. Jones, K. E., Angielczyk, K. D. & Pierce, S. E. Stepwise shifts underlie evolutionary trends in morphological complexity of the mammalian vertebral column. *Nature Commun.* **10**, 5071 (2019).
6. Faure-Brae, M. G. & Cubo, J. Were the synapsids primitively endotherms? A palaeohistological approach using phylogenetic eigenvector maps. *Phil. Trans. R. Soc. B* **375**, 20190138 (2020).
7. Crompton, A. W. et al. Structure of the nasal region of non-mammalian cynodonts and mammaliaforms: speculations on the evolution of mammalian endothermy. *J. Vertebr. Paleontol.* **37**, e126916 (2017).
8. Bajdek, P. et al. Microbiota and food residues including possible evidence of pre-mammalian hair in Upper Permian coprolites from Russia. *Lethaia* **49**, 455–477 (2016).
9. Farmer, C. G. Parental care, destabilizing selection, and the evolution of tetrapod endothermy. *Physiology* **35**, 160–176 (2020).
10. Rey, K. et al. Oxygen isotopes suggest elevated thermometabolism within multiple Permo-Triassic therapsid clades. *eLife* **6**, e28589 (2017).
11. Newham, E., Gill, P. G. & Corfe, I. J. New tools suggest a middle Jurassic origin for mammalian endothermy: advances in state-of-the-art techniques uncover new insights on the evolutionary patterns of mammalian endothermy through time. *BioEssays* **44**, 2100060 (2022).
12. Angielczyk, K. D. & Schmitz, L. Nocturnality in synapsids predates the origin of mammals by over 100 million years. *Proc. R. Soc. B* **281**, 20141642 (2014).
13. Botha, J. & Huttenlocker, A. In *Vertebrate Skeletal Histology and Paleohistology* (eds. de Buffrénil, V. et al.) 550–563 (CRC Press, 2021).
14. Grigg, G. et al. Whole-body endothermy: ancient, homologous and widespread among the ancestors of mammals, birds and crocodylians. *Biol. Rev.* **97**, 766–801 (2022).
15. Benoit, J. et al. The sixth sense in mammalian forerunners: variability of the parietal foramen and the evolution of the pineal eye in South African Permo-Triassic eutheriodont therapsids. *Acta Palaeontol. Pol.* **61**, 777–789 (2016).
16. Benoit, J., Manger, P. R. & Rubidge, B. S. Palaeoneurological clues to the evolution of defining mammalian soft tissue traits. *Sci. Rep.* **6**, 25604 (2016).
17. Rowe, T. B., Macrini, T. E. & Luo, Z.-X. Fossil evidence on origin of the mammalian brain. *Science* **332**, 955–957 (2011).
18. Rabbitt, R. D., Damiano, E. R. & Grant, J. W. In *The Vestibular System* (eds. Highstein, S. M. et al.) 153–201 (Springer, 2004).
19. David, R. et al. Assessing morphology and function of the semicircular duct system: introducing new in-situ visualization and software toolbox. *Sci. Rep.* **6**, 32772 (2016).
20. Highstein, S. M., Fay, R. R. & Popper, A. N. *The Vestibular System* (Springer, 2004).
21. Angelaki, D. E. & Cullen, K. E. Vestibular system: the many facets of a multimodal sense. *Annu. Rev. Neurosci.* **31**, 125–150 (2008).
22. Fitzpatrick, R. C., Butler, J. E. & Day, B. L. Resolving head rotation for human bipedalism. *Curr. Biol.* **16**, 1509–1514 (2006).
23. Ten Kate, J. H. & Kuiper, J. W. The viscosity of the Pike's endolymph. *J. Exp. Biol.* **53**, 495–500 (1970).
24. Oman, C. M. In *The Vestibular System: Function and Morphology* (ed. Gualtierotti, T.) 251–274 (Springer, 1981).
25. Garland, T. & Albuquerque, R. L. Locomotion, energetics, performance, and behavior: a mammalian perspective on lizards, and vice versa. *Integr. Comp. Biol.* **57**, 252–266 (2017).
26. Hirt, M. R. et al. A general scaling law reveals why the largest animals are not the fastest. *Nat. Ecol. Evol.* **1**, 1116–1122 (2017).
27. Jones, G. M. & Spells, K. E. A theoretical and comparative study of the functional dependence of the semicircular canal upon its physical dimensions. *Proc. R. Soc. Lond. B* **157**, 403–419 (1963).
28. Scotese, C. R., Song, H., Mills, B. J. & van der Meer, D. G. Phanerozoic paleotemperatures: the earth's changing climate during the last 540 million years. *Earth Sci. Rev.* **215**, 103503 (2021).
29. Storey, K. B. & Storey, J. M. Metabolic rate depression and biochemical adaptation in anaerobiosis, hibernation and estivation. *Quart. Rev. Biol.* **65**, 145–174 (1990).
30. Legendre, L. J. & Davesne, D. The evolution of mechanisms involved in vertebrate endothermy. *Phil. Trans. R. Soc. B* **375**, 20190136 (2020).
31. Woodley, R. & Buffenstein, R. Thermogenic changes with chronic cold exposure in the naked mole-rat (*Heterocephalus glaber*). *Comp. Biochem. Phys. A* **133**, 827–834 (2002).
32. Pianka, E. R. In *Ecology and Natural History of Desert Lizards: Analyses of the Ecological Niche and Community Structure* (ed. Pianka, E. R.) 35–47 (Princeton Univ. Press, 1986).
33. Grigg, G. C., Beard, L. A. & Augée, M. L. The evolution of endothermy and its diversity in mammals and birds. *Physiol. Biochem. Zool.* **77**, 982–997 (2004).
34. Bennett, A. F. & Ruben, J. A. Endothermy and activity in vertebrates. *Science* **206**, 649–654 (1979).
35. Spoor, F. The semicircular canal system and locomotor behaviour, with special reference to hominin evolution. *Cour. Forschungsinst. Senckenberg* **243**, 93–104 (2003).
36. Kemp, A. D. & Christopher Kirk, E. Eye size and visual acuity influence vestibular anatomy in mammals. *Anat. Rec.* **297**, 781–790 (2014).
37. Money, K. E. et al. Physical properties of fluids and structures of vestibular apparatus of the pigeon. *Am. J. Physiol.* **220**, 140–147 (1971).
38. Rowe, T. Definition, diagnosis, and origin of Mammalia. *J. Vertebr. Palaeontol.* **8**, 241–264 (1988).
39. Nicol, S. C. Energy homeostasis in monotremes. *Front. Neurosci.* **11**, 195 (2017).
40. Spoor, F. & Thewissen, J. G. M. In *Senses on the Threshold: Adaptations in Secondarily Aquatic Vertebrates* (eds Thewissen, J. G. M. & Nummela, S.) 257–286 (Univ. California Press, 2008).
41. Opiang, M. D. Home ranges, movement, and den use in long-beaked echidnas, *Zaglossus bartoni*, from Papua New Guinea. *J. Mammal.* **90**, 340–346 (2009).
42. Viglietti, P. A. et al. Evidence from South Africa for a protracted end-Permian extinction on land. *Proc. Nat. Acad. Sci. USA* **118**, e2017045118 (2021).
43. Jones, K. E. et al. Regionalization of the axial skeleton predates functional adaptation in the forerunners of mammals. *Nature Ecol. Evol.* **4**, 470–478 (2020).
44. Lautenschlager, S. et al. The role of miniaturization in the evolution of the mammalian jaw and middle ear. *Nature* **561**, 533–537 (2018).
45. Donnelly, H. T. Oxygen consumption, activity and body fat in normal and hairless mice. *Lab. Animals* **16**, 167–171 (1982).
46. Bal, N. C. & Periasamy, M. Uncoupling of sarcoendoplasmic reticulum calcium ATPase pump activity by sarcoplakin as the basis for muscle non-shivering thermogenesis. *Phil. Trans. R. Soc. B* **375**, 20190135 (2020).
47. Rowland, L. A., Bal, N. C. & Periasamy, M. The role of skeletal-muscle-based thermogenic mechanisms in vertebrate endothermy. *Biol. Rev.* **90**, 1279–1297 (2015).
48. Benson, R. B., Butler, R., Close, R. A., Saupe, E. & Rabosky, D. L. Biodiversity across space and time in the fossil record. *Curr. Biol.* **31**, R1225–R1236 (2021).
49. Close, R. A. et al. Diversity dynamics of Phanerozoic terrestrial tetrapods at the local-community scale. *Nat. Ecol. & Evol.* **3**, 590–597 (2019).
50. Fernandez, V. et al. Synchrotron reveals Early Triassic odd couple: injured amphibian and aestivating therapsid share burrow. *PLoS ONE* **8**, e64978 (2013).

Publisher's note Springer Nature remains neutral with regard to jurisdictional claims in published maps and institutional affiliations.

© The Author(s), under exclusive licence to Springer Nature Limited 2022

Methods

Comparative inner ear sample

Three inner ear datasets were analysed for 341 species: 3D bony, 3D membranous, and 2D membranous (Supplementary Methods, 'Sampling rationale'). The 3D bony sample consists of 3D endocasts of bony semicircular canals (SC) of 234 extant species (7 amphibians, 67 lepidosaurs (69 specimens), 6 turtles, 9 crocodilians, 72 birds and 73 mammals), and 64 extinct species (1 diadectomorph, 3 non-saurian reptiles, 1 archosauromorph, 2 non-therapsid synapsids, 5 non-neotherapsid therapsids (6 specimens), 16 anomodonts (19 specimens), 5 gorgonopsians, 6 thecocephalians (7 specimens), 9 non-probaenognathian cynodonts (11 specimens), 3 non-mammaliamorph probaenognathians, 9 non-mammalian mammaliamorphs (11 specimens) and 4 mammals). We used non-synapsid fossils to test the method outside the clade of interest at deep divergence time points. The 3D membranous sample consists of 3D endocasts of membranous semicircular ducts (SD) of 50 extant species (1 crocodilian, 9 birds, 3 lepidosaurs, 1 turtle⁵¹, 30 mammals, 3 amphibians⁵² and 3 fishes^{53–55}). Except for fishes, the corresponding bony endocasts of these specimens are part of the 3D bony sample. The 2D membranous sample consists of published photographs^{56–61} and measurements²⁷ of membranous labyrinths of 40 extant fish species (19 chondrichthyans and 21 actinopterygians). The lists of specimens and measurements are provided in Supplementary Data 2.

Data acquisition and processing

The SC endocasts in the 3D bony sample were downloaded from <https://www.morphosource.org/> or segmented using Amira 5.3.3 (Visage Imaging and Konrad-Zuse-Zentrum) from existing and new computed tomography (CT) images obtained with μ CT, or propagation phase-contrast synchrotron microtomography (Extended Data Fig. 1). Segmentation was based on the contrast between bone and air for extant specimens, but was conducted manually for fossils. A wax endocast model of *Dimetrodon* sp. (FMNH PR 4976) was digitized using photogrammetry (Supplementary Note 3). The endocasts of SDs and SCs in the 3D membranous sample were segmented from μ CT scans of the ear region of extant specimens, acquired from autopsies or museum collections and prepared as described previously for membranous labyrinths of 40 extant fish. Segmentation and additional processing¹⁹ was done in Avizo 7.1 (Visualization Science Group) and Geomagic Studio 12 (Raindrop Geomagic). Further information about the specimens and scans are given in Supplementary Data 3.

Measurements of 3D specimens

Four linear measurements were taken per SC for all specimens in the 3D bony and membranous samples: two-dimensional length of the slender portion of membranous labyrinths of 40 extant fish, cross-sectional diameter and major and minor axes of each SC (Extended Data Fig. 2). These functionally relevant measurements mirror SD metrics and were designed for ease of measurement. The length of the slender portion is taken on the SD midline, which is closer to the outermost wall of the SC^{19,62,63}, from the ampullar junction of the SD to the common crus or vestibule (Extended Data Fig. 2). The distal part of the slender portion of the lateral canal is often fused with the vestibule, especially in ectothermic taxa, and ends at the common crus wall. The major and minor axes are taken perpendicular to each other, following the ellipse that best fits the SD torus. They do not follow anatomical landmarks but their endpoints are placed on the SD midline (Extended Data Fig. 2). The radius of curvature and eccentricity of each SC torus was calculated from the semi-minor and semi-major axes, respectively taken as half the measured minor and major axes (Supplementary Methods, 'Biomechanics'). Measurements were taken five times and averaged to reduce error. Measurements of major and minor axes of the SC were taken using the 'straight line' tool of ImageJ⁶⁴, on scaled screenshots from Amira or Avizo, where the screen plane was aligned to the plane

of each SC. Measurements of lengths of slender portions¹⁹ were taken on the same screenshots, using the 'segmented line' tool of ImageJ. SC planes were approximated visually before taking screenshots. A comparison with a more accurate method, which uses landmarks placed along each canal to find the best fitting SC planes, was made in XLSTAT 2018.1.1⁶⁵, no significant differences were found (paired Student *t*-test, $n = 6$, $P = [0.054–0.93]$, two-tailed). The cross-sectional diameter of each SC was measured in Amira, using the SurfaceThickness tool, by selecting five distant points along the slender portion of the SC perpendicular to its plane and averaging their values (Extended Data Fig. 2). Cross-sectional diameters of problematic fossil specimens (for example, showing obvious segmentation artefacts) were measured using the 'straight line' tool of ImageJ on scaled screenshots where the plane of the SC was placed perpendicular to the screen plane. Seven fossil specimens (FMNH UR 161, BPI/1/375, MCZ 1161, GPIT/RE/7119, NHCC LB631, NHCC LB178 and NHCC LB387) had incomplete SCs. We estimated missing measurements of these specimens in R v.4.0.3⁶⁶ with pls 2.7–3⁶⁷, using cross-validated partial least-square regressions on a set of 281 species with all measurements (Supplementary Data 2). Reproducibility was assessed in XLSTAT 2018.1.1 by comparing measurements taken by R.A. and R.D. on a subsample of 77 specimens. All 12 variables are left-skewed, and a two-tailed Kolmogorov–Smirnov test showed no significant difference ($P = [0.404–1.000]$). Repeatability was tested by comparing measurements taken by R.A. and showed no significant intraobserver variation (repeatability scoring between 2.14 to 8.67%; signal to noise ratio minimum of 16.254 where a value of greater than 5 is considered adequate, Supplementary Data 5).

Morphological and functional analyses of the 3D membranous sample were performed using Ariadne Toolbox¹⁹. Input data included surfaces and linesets representing individual components of the duct system (for example, slender parts and ampullae, and modelled cupulae¹⁹). The average height of each cilia area was measured on the μ CT scans. Endolymph density was taken as 1,000 kg m^{−3}, Poisson ratio as 0.48 and cupula shear modulus as 1.44 Pa¹⁹. Output parameters included, among others, wall shape factor, 3D length and cross-sectional area of the slender portion of each SD, enclosed area of the projection of each SD torus on its maximal response plane, and a transfer factor linking endolymph volume displacement to cilia deflection (hereafter called cilia deflection factor). The cilia deflection factor corresponds to the ratio between average deflection of the cupula at the level of the height of the underlying cilia to the average endolymph volume displacement for a given angular head rotation. For specimens for which we have membranous labyrinths, the deflection of the cupula at the level of the height of the underlying cilia has been simulated through finite element analysis¹⁹. The cupula, generally not visible, has been modelled as an extrusion of the crista ampullaris towards the roof of the cupula. Such modelling of cupula anatomy has been confirmed to closely match the actual morphology of the cupula in *Saimiri sciureus* (see Ariadne Manual Data Preparation¹⁹, pages 31–58). Cilia deflection factors of published specimens^{51–55} were estimated from average cupula thickness and cross-sectional area of the ampulla above the crista, following allometric regressions (Supplementary Note 2, models 1–6).

Measurements of 2D images

The 2D membranous sample consists of published photographs^{56–61} and measurements²⁷ of membranous labyrinths. We used ImageJ to process photographs and measure areas enclosed by SD tori, major and minor axes, lengths of slender portions, and inner duct radii (Supplementary Data 2). Photographs were generally taken in lateral view and show the planes of the anterior and posterior SDs at an angle, projected onto the sagittal plane. The resulting distortion can be corrected by multiplying the horizontal axis of the image by 1/cosine of the angle of a specific duct, providing a good representation of undistorted size and shape. Where available, the angles of the planes of the anterior and posterior ducts to the sagittal plane were measured in 'dorsal' view. For specimens

without a 'dorsal' view, we generally used an angle of 45° to undistort the views (Supplementary Data 2). The undistorted views of the anterior and posterior ducts were used to measure corresponding SDs. When a 'dorsal' view was available, measurements for the lateral SD were done on this view. For specimens without a 'dorsal' view, the maximum distance measured between any points on the lateral semicircular duct in lateral view was taken as its major axis. Missing measurements were estimated in R, using cross-validated partial least-square regressions on a set with all measurements (Supplementary Data 2).

Body temperature, body size and phylogeny

Body temperatures of extant species were obtained from the literature (Supplementary Data 2), supplemented by Traitbank (<https://eol.org/traitbank>). For ectothermic taxa, preferred T_b were chosen. When both activity and preferred ranges of T_b were provided, we took the average of the latter. In a few instances (11 ectotherm species) we used online pet care information to estimate preferred T_b . Values for fish species were obtained from FishBase (<http://www.fishbase.org>).

Three body size variables were used: condylobasal length, condylo-anteroorbital length and body mass. Condyllobasal length (posteriormost border of the occipital condyle(s) to the anteriormost tip of the snout, projected onto the sagittal plane) was used to represent cranial size and could be measured for most specimens (Supplementary Data 2). To avoid bias introduced by snout lengths that are either exceptionally long (for example, gharials) or short (for example, anomodonts), we defined the condylo-anteroorbital length as the linear distance from the posteriormost border of the occipital condyle(s) to the anteriormost border of the orbit, projected onto the sagittal plane (see measurements in Supplementary Data 2). Body mass was measured whenever possible (Supplementary Data 2). We used typical adult values rather than extremes, and male and female values were averaged for sexually dimorphic species. For fossils and some specimens of the 3D bony sample, body mass was predicted using an allometric multiple regression of body mass and condylobasal and condylo-anteroorbital lengths (Supplementary Note 2, model 7). Predictions were refined by computing phylogenetically informed body mass residuals.

The phylogeny used in this study (Supplementary Data 6) was built in Mesquite 3.5⁶⁸, using relationships and divergence dates between extant taxa provided by TimeTree⁶⁹ (<http://www.timetree.org>) as a backbone to which extinct clades and species were connected. Relationships at the level of Neoaves were modified from TimeTree to fit assumptions of other published accounts^{70,71}. Relationships and divergence dates of actinopterygians and chondrichthyans that were not covered by TimeTree were obtained from the literature^{72–74}. The reasoning behind phylogenetic relationships, divergence dates, and last occurrence data is detailed in Supplementary Note 4 and follows best practices⁷⁵.

Defining the thermo-motility index

SDs are filled with a fluid (endolymph), whose inertia leads to the deflection of the cupula during head rotation. This deflection generates a signal that is integrated in the brain and is key to essential body functions^{18,19–22}. SDs are angular velocity transducers that are most effective when the signal is unsaturated⁷⁶ and in phase with angular velocity of head motion¹⁸. This only happens for a specific detection range of angular velocities and a specific frequency bandwidth of rotations¹⁸, each bracketed by lower and upper limits. Consequently, the angular velocity range and frequency spectrum of naturally occurring angular head motion is expected to fall within the detection range and frequency bandwidth of SDs. Here we particularly focus on the maxima of angular head motion and semicircular duct function (that is, upper corner frequency and saturating angular velocity, Supplementary Methods, 'Biomechanics'), because it is likely that accurately capturing high angular head motion during the most intense locomotory behaviours is most important for selective fitness of the organism.

Body temperature directly affects the viscosity of the endolymph, such that it decreases when T_b increases^{23,24}. For an organism with a given endolymph composition and SDS morphology, an increase in T_b will result in a reduction of the upper corner frequency and saturating angular velocity. If the SDS morphology does not change or endolymph composition remains stable, the upper limits of angular head motion frequency or velocity will likely fall outside the range of effective SDS function, affecting adversely the selective fitness of the organism. Alternatively, the organism could adapt to more sluggish behaviours, but empirical evidence suggests that, if anything, increased T_b correlates to increased locomotor activity^{25,26,34} (Supplementary Data 1 and Supplementary Note 2). Thus, analysing the maximum SDS function of extinct species should allow us to track changes in T_b , and the acquisition of endothermy. Therefore, we derive the TMI from SDS morphology and endolymph composition, using equations governing the saturating angular velocity and the upper corner frequency, but excluding T_b (Supplementary Methods, 'Biomechanics'). Consequently, when T_b increases, compensatory changes in the TMI, traceable in fossils, are required to keep semicircular duct function constant.

In practice, as fossils do not preserve the membranous labyrinth, we need to predict the morphology of their SDS. To do so, we first used a dataset of 50 species (Supplementary Data 2), for which we had bony and membranous labyrinths, to regress morphometrical parameters of the ducts (including their cross-sectional area) against morphometric parameters of the bony canals (Supplementary Note 2, models 8–19). Next, we used these regressions to obtain fitted values of these duct parameters using morphometric parameters of the bony canals of fossil specimens. Finally, we estimated the residual parameters of the SDS for the fossil specimens through ancestral state estimation, using the phylogeny mentioned above. Similarly, direct information on endolymph viscosity is lacking in fossils. Data on endolymph viscosity at a given temperature has been published for only eight species (one bird, two mammals, five euteleosts)^{23,37,77–82}. Using published data, we calculated the physicochemical component of the TMI of these species (Supplementary Methods, 'Biomechanics') and found that, except for *Columba livia* and *Pleuronectes platessa*, they have endolymph with low viscosity, close to that of water (Extended Data Fig. 4). The phylogenetic distribution of the physicochemical component of the TMI in available species indicates that low-viscosity endolymph was the basal condition for Euarchontoglires and Euteleostei, thus parsimoniously the basal condition for Osteichthyes as well. This phylogenetic context allows us to assume a priori that the physicochemical component of the TMI of synapsid species did not differ from the basal condition. Following these observations, a low-viscosity endolymph was chosen for all species analysed in this study, except birds and pleuronectids. For non-avian diapsids, amphibians, and chondrichthyans, theoretical and empirical relationships between the TMI and T_b are consistent suggesting, *a posteriori*, the retention of low-viscosity endolymph in these taxa (Fig. 2 and Supplementary Methods). Finally, because the TMI scales allometrically, it needs to be corrected for body size when comparing between species (Supplementary Note 2, models 26–31).

A more comprehensive introduction to the biomechanics of the TMI and its complete mathematical derivations are available in Supplementary Methods, 'Biomechanics'. Moreover, a step-by-step protocol describing how to obtain the TMI from bony or membranous morphology is also provided in the Supplementary Methods. A complete description of the statistics related to the computation of the TMI and related analyses is available in Supplementary Note 2.

Statistical analyses

Computation of the TMIs and statistical analyses were done in R using the packages phytools 0.7–70⁸³, caper 1.0.1⁸⁴, geiger 2.0.7⁸⁵, phangorn 2.5.5⁸⁶, Rfast 2.0.1⁸⁷, phylogram 2.1.0⁸⁸, ape 5.5⁸⁹, effectsize 0.5⁹⁰, outliers 0.14⁹¹, motmot 2.1.3⁹² and dplyr 0.7.6⁹³. P -values were

corrected by controlling the false discovery rate (fdr method). Results of tested assumptions and related statistics are reported for all models (Supplementary Note 2).

To determine the morphological parameters of the bony anterior SC (for example, cross-sectional radius and length of the slender portion, radius of curvature and eccentricity) that carry the most information about the transition toward endothermy in the synapsid lineage, we regressed size-corrected morphological parameters on the TMI using PGLS regressions (Supplementary Note 2, models 49–56).

To assess which model best fit the evolution of the TMI, we fitted nine evolutionary models on the TMI (for example, Brownian motion, early burst) and compared their corrected Akaike information criteria (Supplementary Note 2, models 58–66). Results suggest that an evolutionary model with Brownian motion along the proposed phylogenetic tree, with branch lengths scaled using a Pagel's λ of 0.50, and a major shift in the rate of evolution along the branch directly leading to Mammaliaformes, is best for explaining the evolution of the TMI (Supplementary Note 2, model 66).

Phylogenetic logistic regressions were fitted to predict the thermoregulatory regime of extant amniote specimens from their TMI (Supplementary Note 2, model 57). The resulting phylogenetic logistic regression was used to predict probabilities of endothermy for each node of the tree and each fossil species, using the corresponding TMI (Fig. 3, Extended Data Fig. 6 and Extended Data Tables 1 and 2). The TMI for each node of the phylogenetic tree was obtained by maximum-likelihood reconstruction of ancestral states under Brownian motion, using TMIs of all tips and the phylogenetic tree reflecting the best evolutionary model. Accuracy of predictions was assessed 100 times by randomly selecting 151 extant species, fitting a phylogenetic logistic regression to predict their thermoregulatory regime from their TMI, using the fitted phylogenetic logistic regression to predict the thermoregulatory regime of 75 extant species that were not used to produce the phylogenetic logistic regression, and comparing outcomes with real thermoregulatory regimes. The thresholds for endothermy and ectothermy were determined by using the probabilities that gave an error rate of 5%.

Multiple additional tests were conducted to assess whether the TMI is free from body size information (Supplementary Note 2, models 38–39) and robust (Supplementary Note 2, models 43–47).

Probability distributions of predicted T_b of fossil species and groups were obtained (1) by using the PGLS regression between T_b (via the temperature ratio) and the TMI for extant clades (Supplementary Note 2, model 41), and (2) by simulating 15,000 times the evolution of residuals of the temperature ratio using Brownian motion on a phylogenetic tree reflecting the best evolutionary model for these residuals (Supplementary Note 2, section 24).

To assess whether our small non-mammaliaform probainognathian sample could have affected our conclusions on the presence of a shift to endothermy at the root of Mammaliaformes, we computed the likelihood of obtaining the mean TMI we report for this group by chance alone, when randomly sampling and averaging three specimens from distributions of higher TMI means (for example, cynognathian-like mean), using standard deviations observed in well-sampled clades (for example, mammals). This experiment has been replicated 10,000 times to obtain likelihood distributions (Supplementary Note 2, section 26).

Post hoc analyses

We investigated whether high/maximum stride and impact frequencies (as a proxy for behaviourally induced angular head motion⁹⁴) were positively correlated to T_b , and if they explained part of the variance of the TMI left unexplained by T_b . To do so, we performed PGLS regressions (Supplementary Note 2, models 84–89), using stride frequency, impact frequency, body mass, and T_b , sampled for 106 taxa. Impact frequencies were obtained from stride frequencies, using multiplying factors estimated from the analysis of gait types (Supplementary Data 1).

Similarly, we assessed if maximum anaerobic speed (as a proxy for behavioural activity) is higher in endotherms than ectotherms, and if it is positively correlated to T_b . To do so, we performed PGLS ANOVA and PGLS regressions (Supplementary Note 2, models 76–80), using maximum anaerobic speeds, body mass, and T_b , sampled in 428 taxa. Data collection followed the same protocols as above and references are provided in Supplementary Data 1.

We explored which thermoregulatory strategies (for example, aestivation) could have been adopted by fossil synapsids predicted as ectotherms, by comparing their predicted T_b to the palaeoclimate of their palaeolocalization (Supplementary Data 4). To do so, we used the temperature curve of Scotese et al.²⁸ to obtain minimum and maximum global average temperatures (GAT) corresponding to the age range of each fossil specimen. These GATs were corrected for the palaeolatitude of each specimen (obtained from the Paleobiology Database: <https://paleobiodb.org/>), using Fig. 7 of Scotese et al.²⁸ to obtain the latitudinal average temperature (LAT). In addition, we reviewed the literature to compile climate types that have been proposed for the palaeolocalization of each sampled specimen^{95–101}. Furthermore, we collected temperature data (for example, summer maximum temperature) for 150 locations and 16 different Köppen climates from <https://weatherspark.com/>. Climate type and LAT were used in R to predict seasonal temperatures at the palaeolocalization of each fossil specimen, with a range of uncertainty. Palaeolocalization temperature and predicted body temperature (Supplementary Note 2) were randomly sampled from corresponding ranges of uncertainty, and compared 1,000 times to address specific questions about thermoregulatory strategies (for example, whether predicted body temperature is higher than the maximum local night temperature—if true the specimen is probably obligatory diurnal). Results from these tests allowed us to compute probabilities for given thermoregulatory strategies to occur.

Reporting summary

Further information on research design is available in the Nature Research Reporting Summary linked to this paper.

Data availability

The raw datasets used in this study are available in the Supplementary Dataset. Links for CT scan datasets and bony labyrinth 3D meshes obtained from <https://www.morphosource.org/> can be found in Supplementary Data 3. Some bird skull measurements and fish lengths were obtained from <https://skullsite.com/> and fishbase.org, respectively (Supplementary Data 2). Time calibrations between most extant species were obtained from timetree.org. Body mass and T_b of some extant species were obtained from <https://eol.org/traitbank> (Supplementary Data 2). Source data are provided with this paper.

Code availability

The R scripts used in this study are available in the Supplementary Dataset.

51. Evers, S. W. et al. Neurovascular anatomy of the protostegid turtle *Rhinochelys pulchriiceps* and comparisons of membranous and endosseous labyrinth shape in an extant turtle. *Zool. J. Linn. Soc.* **187**, 800–828 (2019).
52. Mason, M. J. et al. The frog inner ear: picture perfect? *J. Assoc. Res. Otolaryngol.* **16**, 171–188 (2015).
53. Schulz-Mirbach, T. et al. A unique swim bladder-inner ear connection in a teleost fish revealed by a combined high-resolution microtomographic and three-dimensional histological study. *BMC Biol.* **11**, 75 (2013).
54. Schulz-Mirbach, T., Heß, M. & Metscher, B. D. Sensory epithelia of the fish inner ear in 3D: studied with high-resolution contrast enhanced microCT. *Front. Zool.* **10**, 63 (2013).
55. Schulz-Mirbach, T., Heß, M. & Plath, M. Inner ear morphology in the Atlantic molly *Poecilia mexicana*—first detailed microanatomical study of the inner ear of a cyprinodontiform species. *PLoS ONE* **6**, e27734 (2011).
56. Ghanem, T. A., Rabbitt, R. D. & Tresco, P. A. Three-dimensional reconstruction of the membranous vestibular labyrinth in the toadfish *Opsanus tau*. *Hearing Res.* **124**, 27–43 (1998).

57. Buran, B. N., Deng, X. & Popper, A. N. Structural variation in the inner ears of four deep-sea elopomorph fishes. *J. Morph.* **265**, 215–225 (2005).

58. Deng, X., Wagner, H. J. & Popper, A. N. The inner ear and its coupling to the swim bladder in the deep-sea fish *Antimora rostrata* (Teleostei: Moridae). *Deep Sea Res.* **58**, 27–37 (2011).

59. Deng, X., Wagner, H. J. & Popper, A. N. Interspecific variations of inner ear structure in the deep-sea fish family Melamphaidae. *Anat. Rec.* **296**, 1064–1082 (2013).

60. Evangelista, C. et al. A comparison of the external morphology of the membranous inner ear in elasmobranchs. *J. Morphol.* **271**, 483–495 (2010).

61. Gauldie, R. W., Mulligan, K. & Thompson, R. K. The otoliths of a chimaera, the New Zealand elephant fish *Callorhynchus milii*. *N. Zeal. J. Mar. Freshw. Res.* **21**, 275–280 (1987).

62. Gray, A. A. *The Labyrinth of Animals: Including Mammals, Birds, Reptiles and Amphibians*, Vol. I (Churchill, 1907).

63. Gray, A. A. *The Labyrinth of Animals: Including Mammals, Birds, Reptiles and Amphibians*, Vol. II (Churchill, 1908).

64. Schneider, C. A., Rasband, W. S. & Eliceiri, K. W. NIH Image to ImageJ: 25 years of image analysis. *Nat. Methods* **9**, 671–675 (2012).

65. XLSTAT statistical and data analysis solution (Addinsoft, 2021).

66. R Core Team. R: a language and environment for statistical computing (R Foundation for Statistical Computing, 2017).

67. Bjørn-Helge, M., Wehrens, R. & Liland, K. H. pls: partial least squares and principal component regression. R package version 2.7-3 (2020).

68. Maddison, W. P. & Maddison, D. R. Mesquite: a modular system for evolutionary analysis, Version 3.61 (2018).

69. Kumar, S. et al. TimeTree: a resource for timelines, timetrees, and divergence times. *Mol. Biol. Evol.* **34**, 1812–1819 (2017).

70. Prum, R. O. et al. A comprehensive phylogeny of birds (Aves) using targeted next-generation DNA sequencing. *Nature* **526**, 569–573 (2015).

71. Suh, A. et al. Ancient horizontal transfers of retrotransposons between birds and ancestors of human pathogenic nematodes. *Nat. Commun.* **7**, 11396 (2016).

72. Naylor, G. J. P. et al. in *Biology of Sharks and Their Relatives* 2 (eds. Carrier, J. C., Musick, J. A. & Heithaus, M. R.) 31–56 (2012).

73. Bakke, I. & Steinar, J. Characterization of mitochondrial ribosomal RNA genes in gadiformes: sequence variations, secondary structural features, and phylogenetic implications. *Mol. Phylogenetics Evol.* **25**, 87–100 (2002).

74. Bakke, I. & Steinar, D. J. Molecular phylogenetics of Gadidae and related Gadiformes based on mitochondrial DNA sequences. *Mar. Biotech.* **7**, 61–69 (2005).

75. Parham, J. F. et al. Best practices for justifying fossil calibrations. *Syst. Biol.* **61**, 346–359 (2012).

76. Rüsch, A. & Thurm, U. Cupula displacement, hair bundle deflection, and physiological responses in the transparent semicircular canal of young eel. *Pflügers Archiv.* **413**, 533–545 (1989).

77. Steer, R. W. *The Influence of Angular and Linear Acceleration and Thermal Stimulation on the Human Semicircular Canal*. Sc.D. thesis, Massachusetts Institute of Technology (1967).

78. Rauch, S. *Biochemie des Hörorgans* (Thieme Verlag, 1964).

79. Ten Doesschate, G. *De eigenschappen van de endolymph van Beenwisse*. Sc. D. thesis, Utrecht University (1914).

80. Money, K. E., Sokoloff, M. & Weaver, R. S. Specific gravity and viscosity of endolymph and perilymph. In NASA, *Second Symposium on the Role of the Vestibular Organs* 91–98 (NASA, 1966).

81. Schnieder, E. A. & Schindler, K. in *Biochemie des Hörorgans* (ed Rauch, S.) 164–168 (Georg Thieme Verlag, 1964).

82. Macdonald, J. A. & Wells, R. M. G. in *Biology of Antarctic fish* (eds di Prisco, G., Maresca, B. & Tota B.) 163–178. (Springer, 1991).

83. Revell, L. J. phytools: An R package for phylogenetic comparative biology (and other things). *Methods Ecol. Evol.* **3**, 217–223 (2012).

84. Orme, D. et al. caper: comparative analyses of phylogenetics and evolution in R. R package version 1.0.1 (2018).

85. Pennell, M. W. et al. geiger v2.0: an expanded suite of methods for fitting macroevolutionary models to phylogenetic trees. *Bioinformatics* **30**, 2216–2218 (2014).

86. Schliep, K. P. phangorn: phylogenetic analysis in R. *Bioinformatics* **27**, 592–593 (2011).

87. Papadakis, M. et al. Rfast: a collection of efficient and extremely fast R functions. R package version 2.0.1 (2020).

88. Wilkinson, S. P. & Davy, S. K. phylogram: an R package for phylogenetic analysis with nested lists. *J. Open Source Softw.* **3**, 790 (2018).

89. Paradis, E. & Schliep, K. ape 5.0: an environment for modern phylogenetics and evolutionary analyses in R. *Bioinformatics* **35**, 526–528 (2019).

90. Ben-Shachar, M., Lüdecke, D. & Makowski, D. effectsize: estimation of effect size indices and standardized parameters. *J. Open Source Softw.* **5**, 2815 (2020).

91. Komsta, L. outliers: tests for outliers. R package version 0.14 (2011).

92. Puttikat M. et al. motmot: models of trait macroevolution on trees. R package version 2.1.3 (2019).

93. Wickham H., François R., Henry L. & Müller K. dplyr: a grammar of data manipulation. R package version 0.7.6 (2018).

94. Xiang, Y., Yakushin, S. B., Kunin, M., Raphan, T. & Cohen, B. Head stabilization by vestibulocollic reflexes during quadrupedal locomotion in monkey. *J. Neurophysiol.* **100**, 763–780 (2008).

95. Boucot A. J., Chen, X., Scotes, C. R. & Morley, R. J. in *SEPM Concepts in Sedimentology and Paleontology*, Vol. 11 (eds Nichols, G. J. & Ricketts, B.) 1–478 (SEPM, 2013).

96. Rees, P. M. et al. Permian phytogeographic patterns and climate data/model comparisons. *J. Geol.* <https://doi.org/10.1086/324203> (2002).

97. Rey, K. et al. Global climate perturbations during the Permo-Triassic mass extinctions recorded by continental tetrapods from South Africa. *Gondwana Res.* **37**, 384–396 (2016).

98. Roscher, M., Stordal, F. & Svensen, H. The effect of global warming and global cooling on the distribution of the latest Permian climate zones. *Palaeogeogr. Palaeoclimatol. Palaeoecol.* **309**, 186–200 (2011).

99. Gibbs, M. T. et al. Simulations of Permian climate and comparisons with climate-sensitive sediments. *J. Geol.* **110**, 33–55 (2002).

100. Harris, R. et al. Climate change during the Triassic and Jurassic. *Geol. Today* **33**, 210–215 (2017).

101. Sellwood, B. W. & Valdes, P. J. Mesozoic climates: general circulation models and the rock record. *Sediment. Geol.* **190**, 269–287 (2006).

Acknowledgements Funding for this project was provided by the Fundação para a Ciência e a Tecnologia postdoctoral fellowship SFRH/BPD/96205/2013, FCT-AGA KHAN Development Network grant number 333206718, National Geographic Society grant number CP-109R-17, the Field Museum, NSF EAR-1337291, the Max Planck Society and the Calleja Foundation. We acknowledge intellectual contributions from discussions with R. Rabbitt. We thank J. White, S. Walsh, P. Campbell, S. Pierce, C. Capobianco, S. Chapman, J. D. Cundiff, A. Wynn, P. Gill, E. Rayfield, J. Hopson, R. Asher, A. Neander, W. Simpson, A. Stroup, A. Resetar, J. Mata, J.-J. Hublin, D. Plotzki, H. Temming, W. van Gestel, J. Jansen, R. Allain, D. Silvestro, F. Condamine, C. Scotes, R. Mundry, S. W. Evers, M. J. Mason, P.-O. Antoine, S. Hellert, C. Schultz, M. B. Soares and A. Schmitt. We also thank the Institute of Veterinary Pathology and the Veterinary Clinic for Birds and Reptiles at Leipzig University, the Leibniz Institute for Zoo and Wildlife Research and the German Primate Center at Göttingen. We acknowledge the MRI platform member of the national infrastructure France-BioImaging supported by the French National Research Agency (ANR-10-INBS-04, «Investments for the future»), the labex CEMEB (ANR-10-LABX-0004) and NUMEV (ANR-10-LABX-0020). IPFN activities received financial support from through projects UIDB/50010/2020 and UIDP/50010/2020. Some silhouettes were obtained from Phylopic.org.

Author contributions R.A., R.D. and K.D.A. designed the study and interpreted the data. R.A. and R.D. collected and analysed the data and wrote the manuscript, with specific input by F.S., K.D.A. and P.M.B. R.D. developed the thermo-motility index and wrote the code. K.D.A. and R.A. reviewed time divergence dates and last occurrence data. R.D., F.S. and A.S. collected specimens for membranous labyrinth analysis. All authors contributed raw and/or processed data, discussed the results, and commented on the draft manuscript.

Competing interests The authors declare no competing interests.

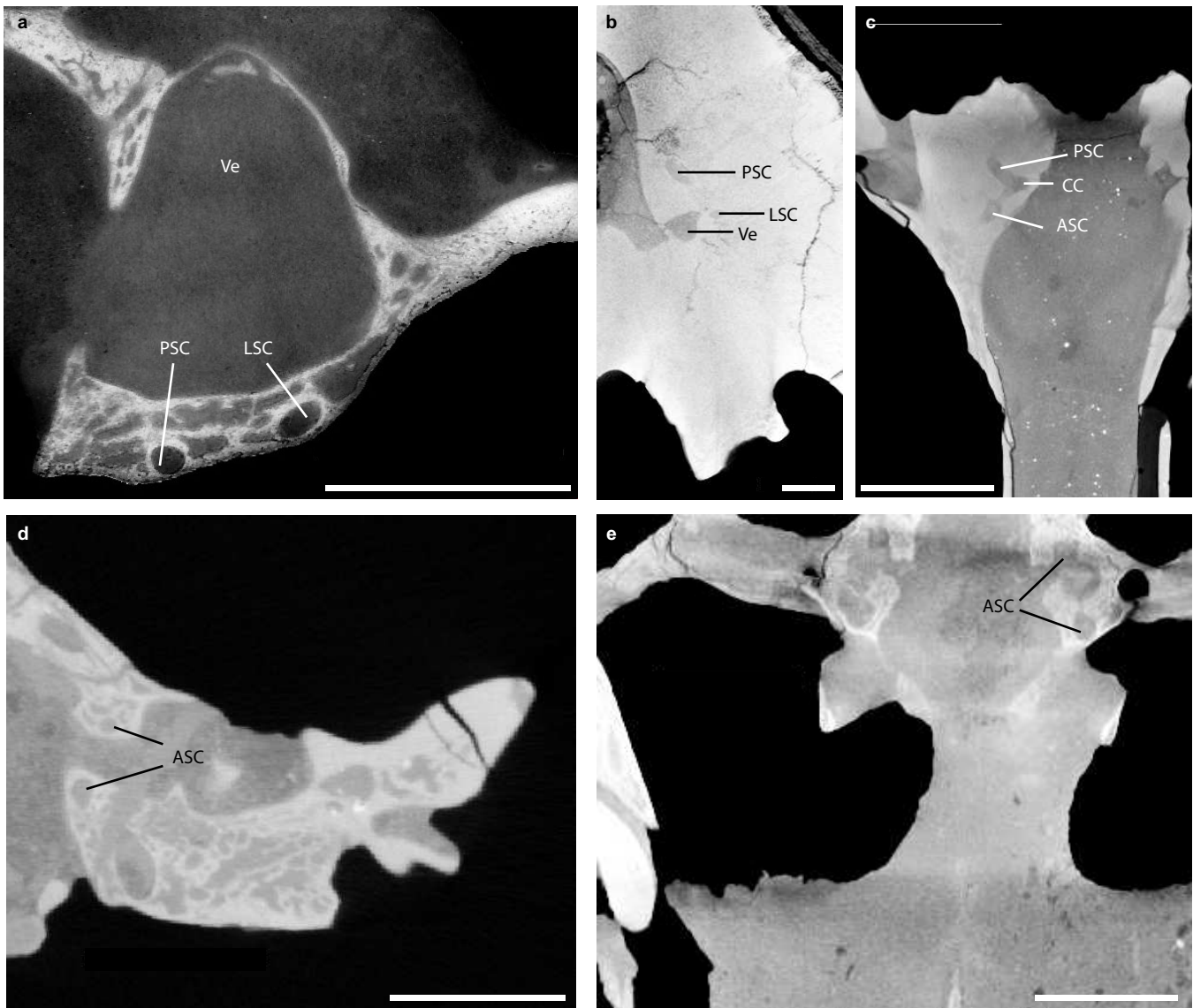
Additional information

Supplementary information The online version contains supplementary material available at <https://doi.org/10.1038/s41586-022-04963-z>.

Correspondence and requests for materials should be addressed to Ricardo Araújo, Romain David or Kenneth D. Angielczyk.

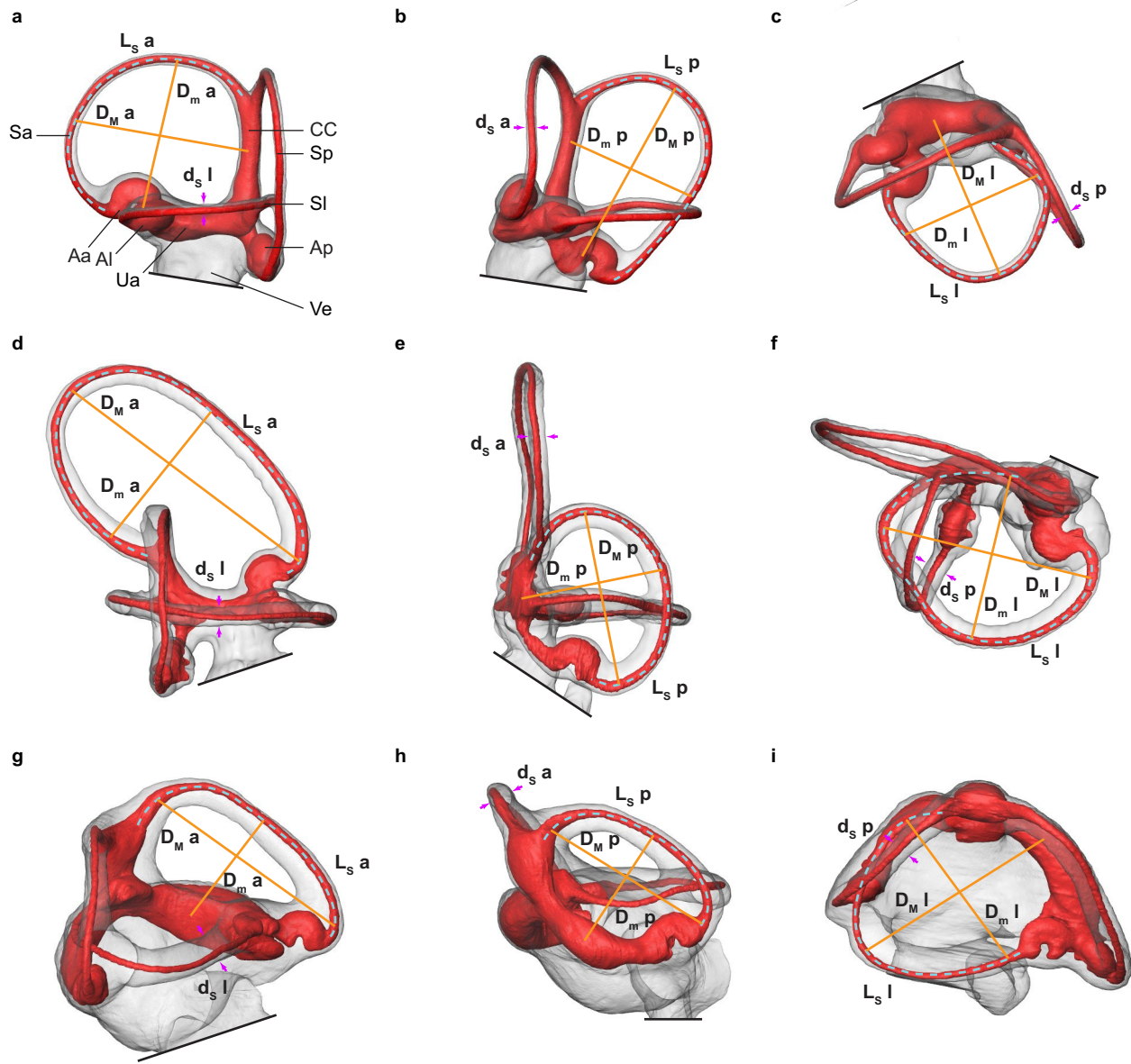
Peer review information *Nature* thanks Michael Benton and the other, anonymous, reviewers for their contribution to the peer review of this work. Peer review reports are available.

Reprints and permissions information is available at <http://www.nature.com/reprints>.



Extended Data Fig. 1 | Selected computed-tomography sections of inner ears of non-mammalian synapsids. **a-e**, Anterior (ASC), posterior (PSC), and lateral (LSC) semicircular canals, vestibule (Ve), and crus communis (CC). Scale bar is 5 mm. **a**, horizontal section of the dicynodont *Kawingasaurus*

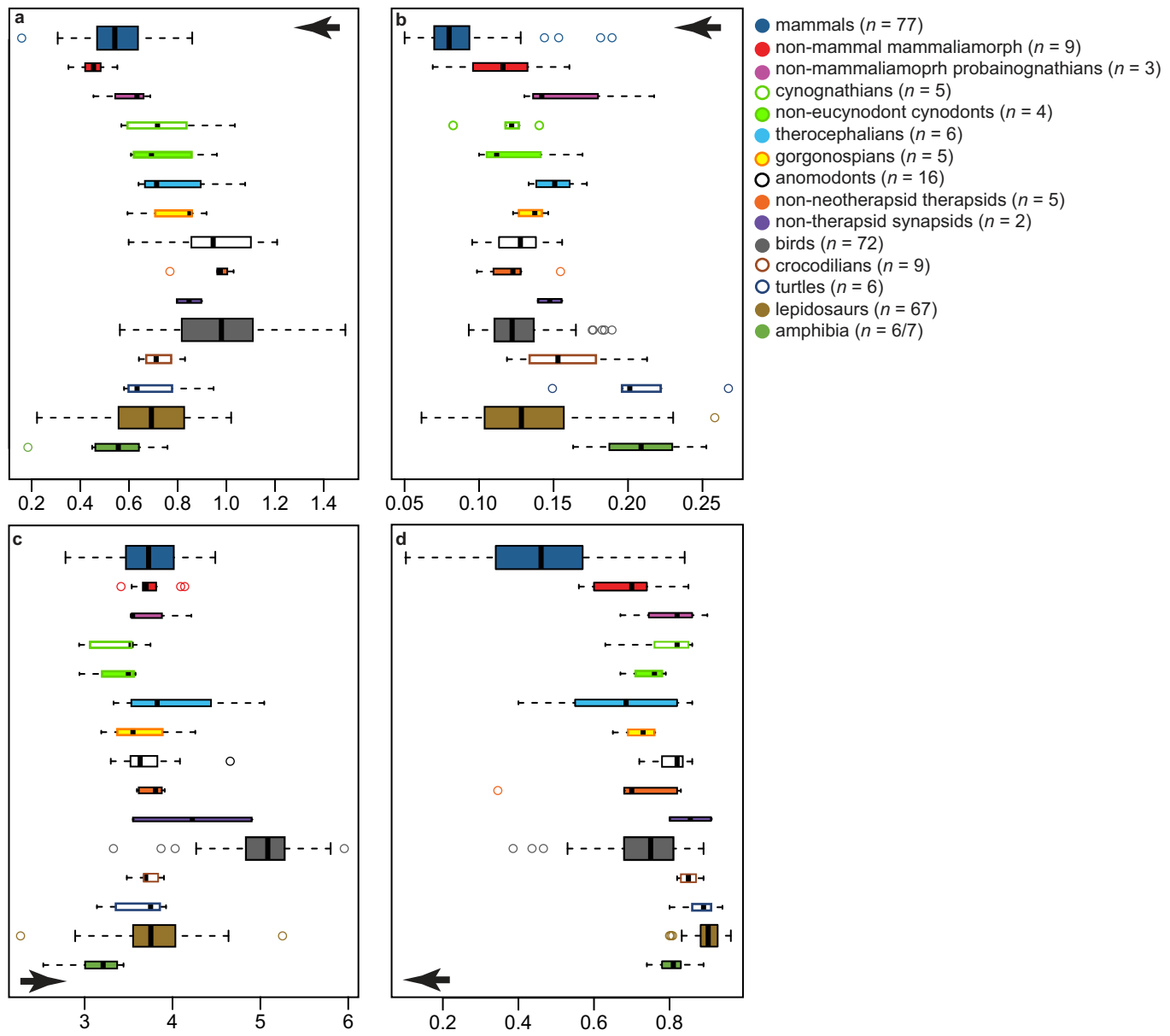
(GPIT/RE/9272). **b**, coronal section of the dicynodont *Aulacephalodon* (NHCC LB335). **c**, horizontal section of the probainognathian *Chiniquodon* (MCZ 3778). **d**, coronal section of the mammaliamorph *Pseudotherium* (PVSJ 882). **e**, horizontal section of the theropcephalian *Mupashi* (NHCC LB44).



Extended Data Fig. 2 | Examples of measurements used in this study.

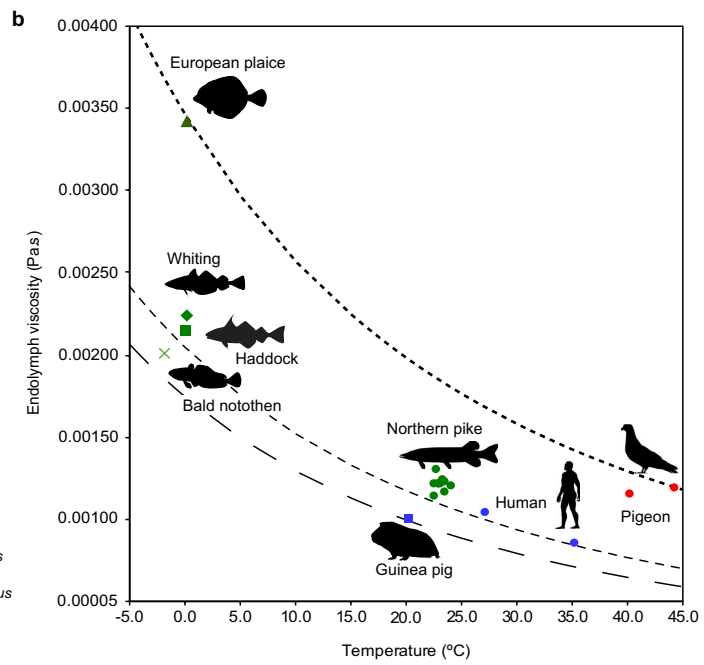
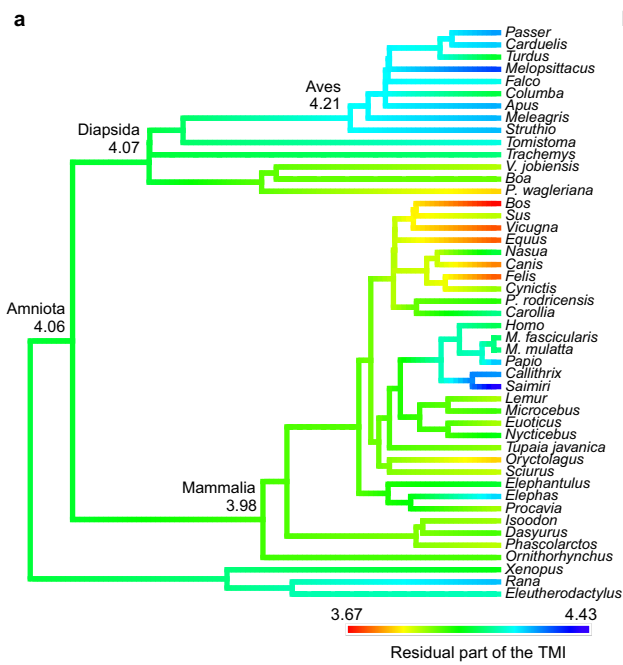
a-i, Views of the bony labyrinth (grey) and the membranous semicircular duct system (red) of an alpaca (**a-c**, CEB130038), a domestic turkey (**d-f**, CEB130069), and a false gharial (**g-i**, CEB140070), in the plane of the anterior (**a, d, g**), posterior (**b, e, h**), and lateral (**c, f, i**) semicircular canals. $D_M a$, $D_M p$, and $D_M l$, major axes of the anterior, posterior, and lateral canal tori; $D_m a$, $D_m p$, and $D_m l$, minor axes of the anterior, posterior, and lateral canal tori; $d_s a$, $d_s p$, and $d_s l$, cross-sectional thicknesses of the slender portion of the anterior, posterior, and lateral canals; $L_s a$, $L_s p$, and $L_s l$, lengths of the slender portion of the anterior, posterior and lateral canals; Sa , Sp , and SI , slender portions of the anterior, posterior, and lateral semicircular ducts; Aa , Ap , and Al , anterior, posterior, and lateral ampullae; Ua , anterior utriculus; CC , common crus; Ve , vestibule.

and $d_s l$, cross-sectional thicknesses of the slender portion of the anterior, posterior, and lateral canals; $L_s a$, $L_s p$, and $L_s l$, lengths of the slender portion of the anterior, posterior and lateral canals; Sa , Sp , and SI , slender portions of the anterior, posterior, and lateral semicircular ducts; Aa , Ap , and Al , anterior, posterior, and lateral ampullae; Ua , anterior utriculus; CC , common crus; Ve , vestibule.



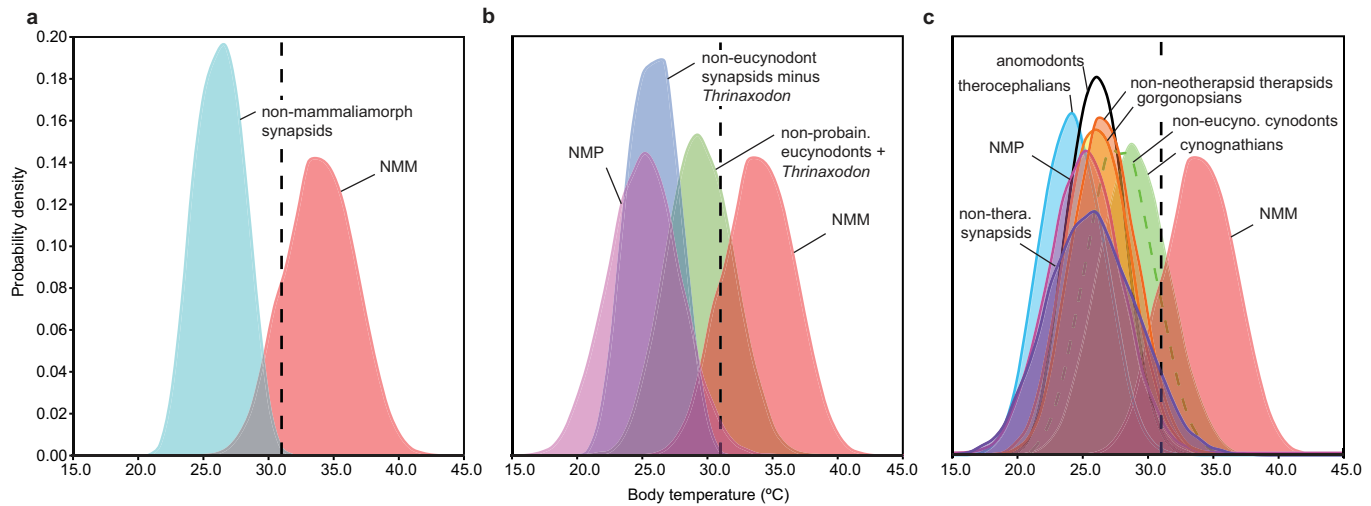
Extended Data Fig. 3 | Distribution of morphological parameters measured on the anterior semicircular canals of tetrapods. a-d. Boxplots of the radius of curvature relative to body mass (a), average cross-sectional thickness (b), and length (c) of the slender portion relative to the radius of curvature, and

eccentricity of the semicircular canal tori (d). Arrows represent the direction of adaptations theoretically expected for endotherms. Boxplot centre, median; box boundaries, first and third quartiles; whiskers, $1.5 \times$ IQR from boundaries. **b.** The outlier *Caecilia* has been omitted to standardize the plot area.



Extended Data Fig. 4 | Phylogenetic distribution of uncontrolled parameters of the TMI. **a**, Optimization of the residual variation of bony/membranous correlations on a time calibrated tree of extant tetrapods. Branch colours reflect the value of the residual variation according to the colour scale. **b**, Scatterplot of endolymph viscosity against T_b showing all data available (see Methods). Mammals are in blue, euteleostean in green

and birds in red. Dashed curves represent endolymph physicochemical properties that are water-like (large dashes), near water-like (medium dashes) or relatively viscous (small dashes). Animal silhouettes were either created by Ricardo Araújo (guinea pig, whiting, haddock, bald notothen) or are available at phylopic (<http://phylopic.org/>) under Public Domain license.

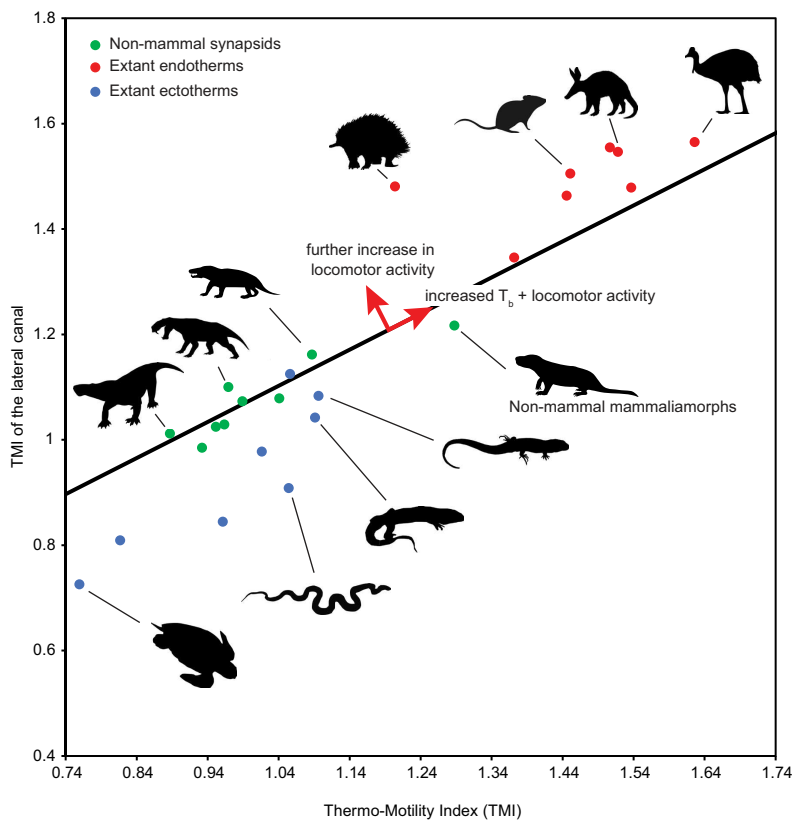


Extended Data Fig. 5 | Probability distributions of body temperatures of fossil synapsids predicted from the TMI. **a-c.** Note the elevated T_b of non-mammalian mammaliamorphs (NMM) and relatively low T_b of non-mammalian synapsids (NMP, **b-c**). Overlaps between distributions should be interpreted carefully because predicted temperatures

are phylogenetically-dependent (see Table 1). Vertical dashed line represents the lowest T_b observed in extant endotherms (31 °C). Predicted T_b for endotherm and ectotherm (**a**), phylogenetic clusters best summarizing the data (**b**), and major groups (**c**) of fossil synapsids. **c.** Note that predicted T_b of non-mammalian synapsids conform to a stochastic process.



Extended Data Fig. 6 | Phylogenetic distribution of the TMI in fossil tetrapods. Optimization of the TMI on a time-calibrated tree of major tetrapod clades and all of the extinct tetrapods analysed in this study. Branch colours reflect the likelihood of being endothermic according to the probability colour scale.



Extended Data Fig. 7 | Relationship between thermo-motility indices of the lateral and anterior canals. The solid line represents the PGLS regression for synapsids. The lateral canal best reflects behavioural agility and its TMI, calculated from the saturating velocity, is the least related to T_b (Supplementary Note 2). Note that non-mammalian synapsids mostly plot above extant ectotherms, suggesting increased locomotor activity for similar T_b . Additionally, while non-mammalian mammaliamorphs plot with

endotherms for the anterior canal TMI (the main TMI used in this study), they are intermediate between endotherms and ectotherms for the lateral canal TMI, suggesting their locomotor activity was intermediate between basal synapsids and mammals. Animal silhouettes were either created by Ricardo Araújo (*Oligokyphus*, *Cynognathia*) or are available at phylopic (<http://phylopic.org/>) under Public Domain license.

Extended Data Table 1 | Probabilities of endothermy for extinct synapsids

Species	Probability	Classification	Species	Probability	Classification
Non-therapsid synapsids					
<i>Eothyris</i>	0.21	Ectotherm	<i>Oliveirosuchus</i>	0.04	Ectotherm
<i>Dimetrodon</i>	0.16	Ectotherm	<i>Euchambersia</i>	0.13	Ectotherm
Non-neotherapsid therapsids					
<i>Hipposaurus</i>	0.50	Uncertain	<i>Mupashi</i>	0.06	Ectotherm
<i>Lemurosaurus</i>	0.11	Ectotherm	<i>Microgomphodon</i>	0.22	Ectotherm
<i>Leucocephalus</i>	0.20	Ectotherm	<i>Choerosaurus</i>	0.24	Ectotherm
<i>Herpetoskylax</i>	0.27	Ectotherm	Non-eucynodont cynodonts		
<i>Moschops</i>	0.16	Ectotherm	<i>Procynosuchus</i>	0.20	Ectotherm
Anomodonts					
<i>Patranomodon</i>	0.21	Ectotherm	<i>Cynosaurus</i>	0.42	Uncertain
<i>Eodicynodon</i>	0.08	Ectotherm	<i>Galesaurus</i>	0.11	Ectotherm
<i>Diictodon</i>	0.29	Ectotherm	<i>Thrinaxodon</i>	0.57	Uncertain
<i>Pristerodon</i>	0.44	Uncertain	Cynognathians		
<i>Niassodon</i>	0.16	Ectotherm	<i>Trirachodon</i>	0.32	Uncertain
<i>Endothiodon bathystoma</i>	0.24	Ectotherm	<i>Cricodon</i>	0.69	Uncertain
<i>Endothiodon tolani</i>	0.10	Ectotherm	<i>Scalenodon</i>	0.34	Uncertain
<i>Abajudon</i>	0.14	Ectotherm	<i>Massetognathus</i>	0.50	Uncertain
<i>Dicynodontoides</i>	0.60	Uncertain	<i>Luangwa</i>	0.10	Ectotherm
<i>Kembawacela</i>	0.48	Uncertain	Non-mammaliamorph probainognathians		
<i>Kawingasaurus</i>	0.27	Ectotherm	<i>Lumkuia</i>	0.18	Ectotherm
<i>Oudenodon</i>	0.06	Ectotherm	<i>Chiniquodon</i>	0.34	Uncertain
<i>Aulacephalodon</i>	0.15	Ectotherm	<i>Riograndia</i>	0.06	Ectotherm
<i>Lystrosaurus declivis</i>	0.10	Ectotherm	Non-mammalian mammaliamorphs		
<i>Lystrosaurus murrayi</i>	0.12	Ectotherm	<i>Tritylodon</i>	0.79	Endotherm
<i>Sangusaurus</i>	0.20	Ectotherm	<i>Oligokyphus</i>	0.69	Uncertain
Gorgonopians					
<i>Scylacocephalus</i>	0.21	Ectotherm	<i>Pseudotherium</i>	0.81	Endotherm
<i>Lycaenops</i>	0.10	Ectotherm	<i>Brasiliodon</i>	0.46	Uncertain
<i>Dixeyia</i>	0.42	Uncertain	<i>Megazostrodon</i>	0.96	Endotherm
BP/1/155	0.26	Ectotherm	<i>Morganucodon watsoni</i>	0.57	Uncertain
GPIT/RE/7124	0.13	Ectotherm	<i>Morganucodon oehleri</i>	0.75	Endotherm
Non-therian mammals					
			<i>Haldanodon</i>	0.67	Uncertain
			<i>Hadrocodium</i>	0.22	Ectotherm
			<i>Dryolestes</i>	0.96	Endotherm

Values above 0.70 are in bold (cross-validated species threshold for endothermy). Fitted probabilities are provided.

Article

Extended Data Table 2 | Probabilities of endothermy for synapsid nodes

Node	Probability	Classification
Mammalia	0.76	Endotherm
<i>Hadrocodium</i> - Mammalia	0.69	Endotherm
<i>Haldanodon</i> - Mammalia	0.70	Endotherm
<i>Morganucodon</i> - Mammalia	0.70	Endotherm
<i>Brasilodon</i> - Mammalia	0.70	Endotherm
<i>Pseudotherium</i> - Mammalia	0.70	Endotherm
<i>Riograndia</i> - Mammalia	0.22	Ectotherm
<i>Chiniquodon</i> - Mammalia	0.23	Ectotherm
<i>Lumkuia</i> - Mammalia	0.24	Ectotherm
<i>Cricodon</i> - Mammalia	0.25	Ectotherm
<i>Thrinaxodon</i> - Mammalia	0.24	Ectotherm
<i>Galesaurus</i> - Mammalia	0.24	Ectotherm
<i>Cynosaurus</i> - Mammalia	0.23	Ectotherm
<i>Procynosuchus</i> - Mammalia	0.23	Ectotherm
<i>Mupashi</i> - Mammalia	0.20	Ectotherm
<i>Dixeyia</i> - Mammalia	0.20	Ectotherm
<i>Diictodon</i> - Mammalia	0.20	Ectotherm
<i>Moschops</i> - Mammalia	0.20	Ectotherm
<i>Hipposaurus</i> - Mammalia	0.20	Ectotherm
<i>Dimetrodon</i> - Mammalia	0.16	Ectotherm
<i>Eothyris</i> - Mammalia	0.15	Ectotherm

Values above 0.53 are in bold (cross-validated clade threshold for endothermy). Fitted probabilities are provided.

Extended Data Table 3 | Probabilities of endothermy for groups of non-mammalian synapsids

Group	Probability	Classification
Non-mammalian mammaliamorphs	0.70	Endotherm
Non-mammaliamorph probainognathians	0.17	Ectotherm
Cynognathians	0.36	Ectotherm
Non-eucynodont cynodonts	0.30	Ectotherm
Therocephalians	0.13	Ectotherm
Gorgonopsians	0.20	Ectotherm
Anomodonts	0.20	Ectotherm
Non-neotherapsids therapsids	0.23	Ectotherm
Non-therapsid synapsids	0.18	Ectotherm

Values above 0.53 are in bold (cross-validated clade threshold for endothermy). Fitted probabilities are provided.

Reporting Summary

Nature Portfolio wishes to improve the reproducibility of the work that we publish. This form provides structure for consistency and transparency in reporting. For further information on Nature Portfolio policies, see our [Editorial Policies](#) and the [Editorial Policy Checklist](#).

Statistics

For all statistical analyses, confirm that the following items are present in the figure legend, table legend, main text, or Methods section.

n/a Confirmed

- The exact sample size (n) for each experimental group/condition, given as a discrete number and unit of measurement
- A statement on whether measurements were taken from distinct samples or whether the same sample was measured repeatedly
- The statistical test(s) used AND whether they are one- or two-sided
Only common tests should be described solely by name; describe more complex techniques in the Methods section.
- A description of all covariates tested
- A description of any assumptions or corrections, such as tests of normality and adjustment for multiple comparisons
- A full description of the statistical parameters including central tendency (e.g. means) or other basic estimates (e.g. regression coefficient) AND variation (e.g. standard deviation) or associated estimates of uncertainty (e.g. confidence intervals)
- For null hypothesis testing, the test statistic (e.g. F , t , r) with confidence intervals, effect sizes, degrees of freedom and P value noted
Give P values as exact values whenever suitable.
- For Bayesian analysis, information on the choice of priors and Markov chain Monte Carlo settings
- For hierarchical and complex designs, identification of the appropriate level for tests and full reporting of outcomes
- Estimates of effect sizes (e.g. Cohen's d , Pearson's r), indicating how they were calculated

Our web collection on [statistics for biologists](#) contains articles on many of the points above.

Software and code

Policy information about [availability of computer code](#)

Data collection

Inner ears obtained from micro-computed tomographies or propagation phase-contrast microtomographies were segmented and measured using Amira 5.3.3, Avizo 7.1, and ImageJ 1.53e. Membranous labyrinths were segmented in Avizo 7.1, prepared for analysis in Geomagic Studio 12, and analysed using Ariadne toolbox v1.1.0. 2D measurements of published membranous labyrinths were obtained following protocols described in the Methods, using ImageJ 1.53e. For some specimens, condylobasal length and condylo-anterorbital length were calculated from scans or photographs using Amira 5.3.3, Avizo 7.1, or ImageJ 1.53e (see Supplementary Data 2 for further details). We used Mesquite 3.5 for constructing the phylogenetic tree and setting the calibration nodes.

Data analysis

We used R v.4.0.3 and XLSAT 2018.1.1 for all analyses performed. The R scripts used in this study are available in the Supplementary Dataset.

For manuscripts utilizing custom algorithms or software that are central to the research but not yet described in published literature, software must be made available to editors and reviewers. We strongly encourage code deposition in a community repository (e.g. GitHub). See the Nature Portfolio [guidelines for submitting code & software](#) for further information.

Data

Policy information about [availability of data](#)

All manuscripts must include a [data availability statement](#). This statement should provide the following information, where applicable:

- Accession codes, unique identifiers, or web links for publicly available datasets
- A description of any restrictions on data availability
- For clinical datasets or third party data, please ensure that the statement adheres to our [policy](#)

The raw datasets used in this study are available in the Supplementary Dataset. Links for CT scan datasets and bony labyrinth 3D meshes obtained from Morphosource.org can be found in Supplementary Data 3. Some bird skull measurements and fish lengths were obtained from skullsite.com and fishbase.org, respectively (Supplementary Data 2). Time calibrations between most extant species were obtained from timetree.org. Body mass and Tb of some extant species were obtained from eol.org/traitbank (Supplementary Data 2).

Human research participants

Policy information about [studies involving human research participants and Sex and Gender in Research](#).

Reporting on sex and gender

N/A

Population characteristics

N/A

Recruitment

N/A

Ethics oversight

N/A

Note that full information on the approval of the study protocol must also be provided in the manuscript.

Field-specific reporting

Please select the one below that is the best fit for your research. If you are not sure, read the appropriate sections before making your selection.

Life sciences

Behavioural & social sciences

Ecological, evolutionary & environmental sciences

For a reference copy of the document with all sections, see nature.com/documents/nr-reporting-summary-flat.pdf

Life sciences study design

All studies must disclose on these points even when the disclosure is negative.

Sample size

Our sample captures taxonomic, phylogenetic, morphological, ecological, behavioural and locomotor diversity, but was constrained by the availability of material. We focused on densely sampling mammals and birds, which we used as independent models for endotherms; we used a large lepidosaurian sample as a model for ectotherms. The remaining extant specimens covered the range of body temperatures in vertebrates, but they are not the focus of this study. Our fossil sample included several mammaliamorphs, where the transition to endothermy is thought to occur. The 2D dataset is less accurate than the 3D sets, but was only used to extend the analysis to lower body temperatures, to obtain a broader range of data to assess the relationship between temperature and the Thermo-Motility Index. Predictions for the thermal regime of fossil synapsids are only based on the 3D sets.

Data exclusions

No data was excluded from the analyses.

Replication

Repeatability and reproducibility tests were successful and respective statistics are available in Supplementary Data 4. Measurements were repeated five times by two different individuals to perform these tests (for further details see Methods).

Randomization

Randomization was used for cross-validation of the logistic regression and partial least-squares regressions used to calculate missing values in fossils. Each of these analyses was replicated 100 times, and for each of them specimens were randomly assigned to training and testing sets. Randomization was not used for the remaining analyses because of the nature of fossil material.

Blinding

Blinding is not relevant to our study due to the nature of the analysis of fossil material.

Reporting for specific materials, systems and methods

We require information from authors about some types of materials, experimental systems and methods used in many studies. Here, indicate whether each material, system or method listed is relevant to your study. If you are not sure if a list item applies to your research, read the appropriate section before selecting a response.

Materials & experimental systems

n/a	Involved in the study
<input checked="" type="checkbox"/>	Antibodies
<input checked="" type="checkbox"/>	Eukaryotic cell lines
<input type="checkbox"/>	Palaeontology and archaeology
<input checked="" type="checkbox"/>	Animals and other organisms
<input checked="" type="checkbox"/>	Clinical data
<input checked="" type="checkbox"/>	Dual use research of concern

Methods

n/a	Involved in the study
<input checked="" type="checkbox"/>	ChIP-seq
<input checked="" type="checkbox"/>	Flow cytometry
<input checked="" type="checkbox"/>	MRI-based neuroimaging

Palaeontology and Archaeology

Specimen provenance

This study uses 352 specimens in total and all details concerning provenance of each specimen is provided in Supplementary Data 2 and 3. No new fossil specimens were obtained in the course of this study, therefore no permits were required to conduct the current study.

Specimen deposition

All specimens are part of collections housed in public museums or institutions and are freely accessible. This study uses 352 specimens in total and all details of the institutions where the specimens are housed are provided in Supplementary Data 2.

Dating methods

No new dates are provided, but the divergence time ages and last appearance data are based on stratigraphical correlation and previously published radiometric data (Supplementary Note 4).

Tick this box to confirm that the raw and calibrated dates are available in the paper or in Supplementary Information.

Ethics oversight

No ethical approval was required because only specimens from public collections were used.

Note that full information on the approval of the study protocol must also be provided in the manuscript.